UNIVERSITY OF CALIFORNIA SAN DIEGO

Quantum Systems of Indirect Excitons in GaAs Heterostructures

A Dissertation submitted in partial satisfaction of the requirements
for the degree Doctor of Philosophy

in

Physics

by

Darius Jamsheed Choksy

Committee in charge:

Professor Leonid Butov, Chair
Professor Michael Fogler
Professor Shayan Mookherjea
Professor Thomas Murphy

2023

The Dissertation of Darius Jamsheed Choksy is approved, and it is acceptable in quality and form for publication on microfilm and electronically.

University of California San Diego

2023

TABLE OF CONTENTS

LIST OF FIGURES

LIST OF ABBREVIATIONS

DX   Direct Exciton

IX   Indirect Exciton

QW   Quantum well

CQW   Coupled Quantum well

PL   Photoluminescence

I-EHP   Indirect electron-hole plasma

BEC   Bose-Einstein condensate

BCS   Bardeen-Cooper-Schrieffer

ACKNOWLEDGEMENTS

I would like to thank my advisor, Leonid Butov for his mentorship and guidance throughout my PhD research. Not only did he excel at explaining complex physical phenomena in a clear and comprehensive manner, but also taught me how to approach and troubleshoot experiments with rigor and precision. I am proud of the work I achieved working in Leonid's group and am grateful for the opportunity to do so.

I would like to thank my colleagues. I am thankful to Chelsey Dorow, Matt Hasling, and Erica Calman for their mentorship as I began my work in the lab. I would like to thank Lewis Fowler-Gerace for his advice and comradery during that time as well. I am thankful to Jason Leonard for the work we did together and his willingness to teach. I am thankful to Erik Szwed for his hard work and dedication on the projects we worked on together and to him and Zhiwen Zhou for taking on the future work in the Butov group.

I would like to thank Chao Xu, Brian Vermilyea, and Michael Fogler for their theoretical contributions to our experimental work. Additionally, I would like to thank the groups of Loren Pfeiffer and Art Gossard for the excellent quality samples used in our experiments.

Finally, I would like to thank my friends and family for their love and support. Whether it was struggling with classes, volunteering for the Young Physicists Program, playing games together, or exploring San Diego, my friends always supported me through the struggles of graduate school. My parents were also always very supportive and encouraging, helping me navigate difficult life challenges. I would also like to thank my partner Katie for being a constant source of joy, love, and support throughout my graduate school career.

Chapter 3, in full, is a reprint of the material as it appears in D. J. Choksy, Chao Xu, M. M. Fogler, L. V. Butov, J. Norman, and A. C. Gossard, Attractive and repulsive dipolar interaction in

bilayers of indirect excitons, *Phys Rev B* **103**, 045126 (2021), where the dissertation author was the first author. The co-authors in these publications directed, supervised, and co-worked on the research which forms the basis of this chapter.

Chapter 4, in full, is a reprint of the material as it appears in D. J. Choksy*, E. A. Szwed*, L. V. Butov, K. W. Baldwin, L. N. Pfeiffer, Fermi edge singularity in neutral electron-hole system, arXiv:2209.06026 (2022), where the dissertation author shares the first authorship. This work is currently being prepared for publication. The co-authors in these publications directed, supervised, and co-worked on the research which forms the basis of this chapter.

VITA

2017   Bachelor of Arts in Physics, The University of Chicago

2019   Master of Science in Physics, University of California San Diego

2023   Doctor of Philosophy in Physics, University of California San Diego

PUBLICATIONS

D. J. Choksy*, E. A. Szwed*, L. V. Butov, K. W. Baldwin, L. N. Pfeiffer. Fermi edge singularity in neutral electron-hole system, arXiv:2209.06026 (2022).

Talk: CLEO 2023: "Fermi edge singularity in ultracold neutral electron-hole plasma." **D. J. Choksy**, E. A. Szwed, L. V. Butov, K. W. Baldwin, and L. N. Pfeiffer, FTh3M.4

Talk: CLEO 2022: "Fermi edge singularity in ultracold neutral electron-hole plasma." **D. J. Choksy**, E. A. Szwed, L. V. Butov, K. W. Baldwin, and L. N. Pfeiffer, FM1A.3

Poster presentation: CLEO 2021: "Dipolar Interactions in Bilayers of Indirect Excitons." **D.J. Choksy**, Chao Xu, M. Fogler, L.V. Butov, J. Norman, A.C. Gossard. JTu3A.37

L. H. Fowler-Gerace, **D. J. Choksy**, L. V. Butov. Voltage-controlled long-range propagation of indirect excitons in van der Waals heterostructure, arXiv:2101.01262 (2021) , Phys. Rev. B 104, 165302 (2021).

D. J. Choksy, Chao Xu, M. M. Fogler, L. V. Butov, J. Norman, and A. C. Gossard. Attractive and repulsive dipolar interaction in bilayers of indirect excitons, arXiv:2011.06084 (2021), Phys. Rev. B 103, 045126. Editor's Suggestion

Poster presentation: CLEO 2020: "Interactions between indirect excitons in separate coupled quantum wells." **D.J. Choksy**, L.V. Butov, J. Norman, and A.C. Gossard. JTh2F.18

E. V. Calman, L. H. Fowler-Gerace, **D. J. Choksy**, L. V. Butov, D. E.Nikonov, I. A. Young, S. Hu, A. Mishchenko, and A. K. Geim. Indirect excitons and trions in MoSe2/WSe2 van der Waals heterostructures, arXiv:1901.08664 (2019), Nano Lett. 20, 1869 (2020).

Poster presentation: CLEO 2019: "High-mobility indirect excitons in a wide single quantum well heterostructure." C.J. Dorow, **D.J. Choksy**, M.W. Hasling, J.R. Leonard, M.M. Fogler, L.V. Butov, K.W. West, L.N. Pfeiffer. JW2A.34

C.J. Dorow, M.W. Hasling, **D.J. Choksy**, J.R. Leonard, L.V. Butov, K.W. West, L.N. Pfeiffer. High-mobility indirect excitons in wide single quantum well, arXiv:1810.01057 (2018), Appl. Phys. Lett. 113, 212102 (2018).

ABSTRACT OF THE DISSERTATION

Quantum Systems of Indirect Excitons in GaAs Heterostructures

by

Darius Jamsheed Choksy

Doctor of Philosophy in Physics

University of California San Diego, 2023

Professor Leonid Butov, Chair

Semiconductors have proven themselves to be an excellent platform for both the development of new technologies and the study of fundamental physics. Various semiconductor materials provide us the ability to control and study the bulk system behavior, electronic behavior, and light-matter interactions.

Of particular interest to this dissertation is the study of a quasi-particle that can form in semiconductors known as an exciton. Made from an electron and hole, it also has very useful photonic properties. In our work we study excitons created by photoexcitation, where a laser excites an electron from the lattice, creating an electron and hole, the electrons and holes created can then form a bound state known as an exciton. Excitons can transform into photons via radiative recombination.

Our experiments typically deal with a system of quantum wells, engineered to keep the electrons and holes spatially separated, a bound pair of an electron and hole with the electron and hole in different quantum wells is known as an indirect exciton. Some of the properties of indirect excitons are an electric dipole moment, energy controlled by voltage, long lifetimes, macroscopic transport, and they are bosons. These properties as well as their interaction with light allow for systems to be created that act as proof-of-concept prototypes for excitonic devices, as well as a platform to study fundamental physics of cold bosons. The work in this dissertation is primarily focused on dipole-dipole attraction and the formation of a Fermi edge singularity in these systems. These works give us new insights into the interactions of bosons and formation of new states of matter.

Chapter 1: Introduction to Indirect Excitons

Predicted by Frenkel in 1931, an exciton is a quasi-particle formed from an electron, photo excited from the valence band to the conduction band, and an electron hole. This bound state can then travel through the lattice [1] [2]. As such excitons can be used to study light-matter interactions and bosons in semiconductors. Due to their low mass, excitons can also form Bose-Einstein condensates at much higher temperatures than atomic systems [3]. Additionally, this light-matter behavior allows for the construction of excitonic devices that directly couple with optical communications. As such excitons provide a useful platform for both the development of devices and study of bosonic interactions [4].

1.1: Coupled Quantum wells

The systems studied in this dissertation are based on a set of coupled quantum wells (CQW) formed of GaAs quantum wells with an AlGaAs barrier. In these systems both direct and indirect excitons form. A direct exciton (DX) is an electron and hole bound in the same GaAs quantum well (QW), while an indirect exciton (IX) is formed from an electron and hole in the spatially separated QW. The GaAs QWs are typically 10nm apart but this separation can be varied. We typically use GaAs and AlGaAs systems as GaAs has a direct bandgap and the processing of GaAs/AlGaAs systems can be done to high precision with few defects.
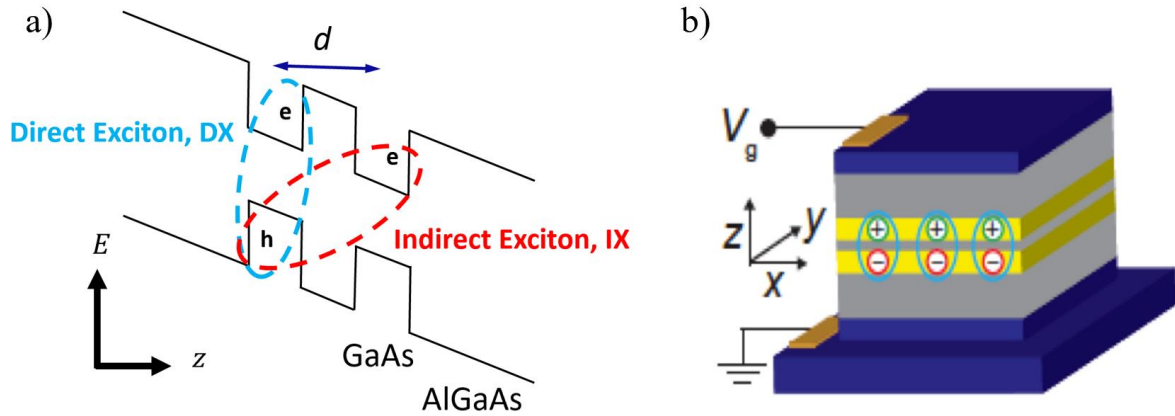
Figure 1.1: a) Couple Quantum well (CQW) energy band diagram with applied voltage to induce the indirect regime. b) Schematic diagram of voltage gates on sample showing CQWs.

Additionally, a voltage gate is applied to the sample such that an electric field can be applied perpendicular to the planes of the quantum wells. This electric field reduces the energy of the IX by edF_z where e is electron charge, d is the separation between the electron and hole layers and F_z is the applied electric field. The energy of DX is $E_{DX} = E_g - E_{b,DX}$ while the energy of the IX is $E_{IX} = E_g - E_{b,IX} - edF_z$ where $E_{b,DX}$ and $E_{b,IX}$ are the binding energy of the DX and IX respectively ($E_{b,IX}$ ~3meV in a 150-40-150nm GaAs/AlAs CQW) and E_g is the bandgap (~1.5eV for GaAs). As such a strong enough electric field $edF_z > E_{b,DX} - E_{b,IX}$ causes the IX to be the energetically favorable state. A schematic of the band diagram can be seen in **Figure 1.1** [5] [6]. Due to this change in energy with an applied electric field we can see a transition from a DX regime to an IX regime with increasing voltage, and can even use the applied voltage to control the IX energy, a shift of IX emission energy vs voltage can be seen in **Figure 1.2**.
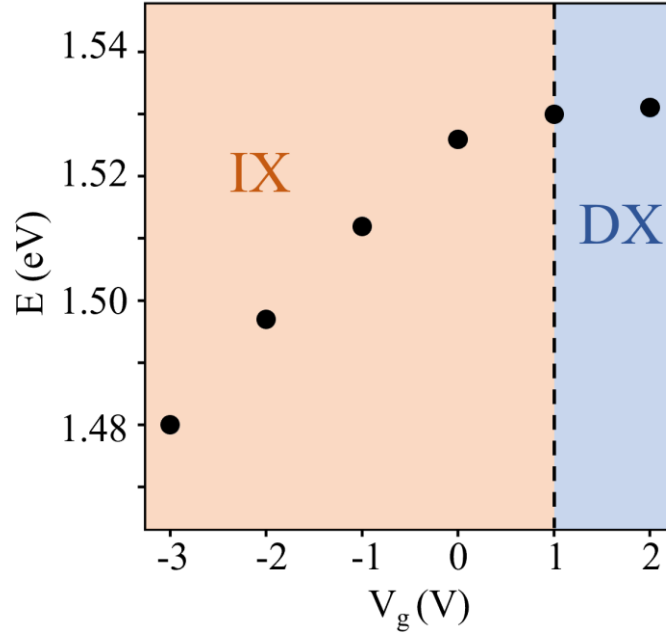
Figure 1.2: Exciton emission energy as a function of applied voltage. Indirect regime is designated in orange and shows a linear shift of the IX photoemission energy with voltage while in the direct regime, designated in blue, the DX photoemission energy is basically unchanged with voltage.

1.2: IX properties

IX Potential Landscape

As discussed in the previous section, the energy of the IX can be tuned and controlled with an applied electric field by - edF_z. We can use these features to design gates such that there are areas in the plane of the CQWs that are more energetically favorable to IXs and thus create IX based devices or environments more suitable for studying fundamental physics. Typically there is a single CQW system through the entire sample. Some examples of excitonic devices are transistors, ramps, and photonic storage devices, while some geometries to better study fundamental physics are traps or split-gate devices [4]. Simply by designing a different shape of electrode on the surface of the heterostructure the potential landscape in the plane parallel to the CQWs can be controlled.

Long lifetime

The application of the electric field and spatial separation of the CQW allows us to control the lifetime of the IX by adjusting the overlap of the electron and hole wave functions. The lifetime of IXs is inversely proportional to the overlap of the electron and hole wavefunctions squared. As such IXs typically have lifetimes from tens of ns to tens of µs, many orders of magnitude larger than the DX lifetime which is on order of tens of ps [7].

Dipole moment

As an IX is a bound pair of an electron and hole with spatial separation, it has a built-in dipole moment. This causes dipolar interactions between neighboring IXs, causing IXs to repel each other in-plane and attract out of plane in certain orientations [8]. Thus, IXs within the same CQW will repel each other and this repulsion increases the IXs energy with increasing density.

Disorder screening

Disorder is the distribution of energy states, and typically interferes with experimental results by adding random changes to the local energy landscape. In the CQW systems described previously disorder is typically due to fluctuations on the QW widths, as the energy of a particle in a QW with width L scales roughly as $1/L^2$, fluctuations in the width of a wider well cause smaller variations in energy [9]. The repulsive interactions between the in-plane IXs can screen disorder in the sample. At lower densities the IXs are relatively localized, but at higher densities this disorder can be screened [10].

Long-range transport

The combination of tunable long lifetimes, repulsive dipole interactions, and disorder screening can lead to macroscopic transport. Experiments have shown that IXs can transport hundreds of microns [11] [12] [13]. This transport allows for the study of the evolution of IX clouds over time, their interactions with other IX clouds, and the construction of macroscopic devices used to facilitate IX transport such as conveyers, stirring potentials, and ramps [4]. Macroscopic transport, much larger than the diffraction limit of optical experimental setups also allows for the study of IXs via spatially and spectrally resolved optical imaging of the photoemission.

Fast cooling

The cooling of hot photoexcited excitons down to the temperature of the cold lattice occurs via emission of bulk longitudinal acoustic phonons. The rate of cooling is about three orders of magnitude faster for excitons in GaAs QWs than bulk GaAs due to relaxation of the momentum conservation law in a direction perpendicular to the QW plane [14] [15] [16] [17]. Additionally, by using pulsed excitation, measuring after the pulse, and by measuring large distances away from the excitation spot (possible due to the longer transport), heating of the exciton system due to the laser excitation can be minimized.

Excitation and density

IXs density can be controlled via laser excitation. By tuning the laser to the DX energy more efficient absorption of exciting photons can occur. This more efficient absorption also reduces heating via the laser. Additionally, by increasing the laser intensity, the density of IXs increases as more photons are absorbed. At increasing density, the repulsion between IXs causes broadening of the emission spectrum [18].

Coherence

Because the temperature of quantum degeneracy is inversely proportional to mass $T_q = 2\pi\hbar^2 n/(m)$ a lower mass results in a higher temperature of quantum degeneracy. The mass of an IX is ~$0.22m_0$ in GaAs CQW with a well width of 80nm and separation of 40nm, where m_0 is the mass of a free electron and as such they have orders of magnitude lower degeneracy temperatures than atomic systems. Spontaneous coherence with coherence length much longer than in a classical gas has been observed in a cold exciton gas [3].

1.3: IXs as a system to study cold bosons

Low mass and density control

IXs excel as a platform for studying cold bosons. An IX's low mass results in relatively high temperatures of quantum degeneracy. Additionally with controllable density the transition between bound hydrogen-like IXs at low density to e-h plasma at high density can be studied. The low density excitonic regime with the density, n, can be described as $n << 1/a_B^D$ where a_B^D is the Bohr radius to the dimension of the system [19]. In the high density, regime $n > 1/a_B^D$ the hydrogen-like IXs dissociate and an e-h plasma forms where excitons can form at the Fermi edge as Cooper pair-like bosons [20].

Bose-Einstein Condensate (BEC) and Bardeen-Cooper-Schrieffer (BCS)

For condensates to form in e-h systems ultracold temperatures are required. The ultracold regime is where the temperature is less than the binding energy and temperature of quantum degeneracy T_q given by $T_q \sim \frac{2\pi\hbar^2}{m_x}n$, the phase diagram for ultracold e-h system is given in **Figure 1.3** [20] [19].

In the low density regime spontaneous coherence and condensation have been observed. The measured first order coherence function and distribution in momentum space agree with theory of a Bose-Einstein Condensate (BEC) of equilibrium bosons, where all of the particles are in the ground state [3]. Other effects in an IX BEC are ordered exciton states [21], commensurability [22], Pancharatnam–Berry phase [23], Interference Dislocations [24], and spin textures [25].

As density increases the IXs dissociate and an e-h plasma forms. In this e-h plasma Cooper pair-like excitons can form. While hydrogen-like excitons form at momentum states close to zero, the Cooper pair-like excitons form close to the Fermi momentum [20].

These Cooper pair-like excitons can form a Bardeen-Cooper-Schrieffer-like (BCS-like) condensate an analogy to super conducting. A requirement for Cooper pair-like exciton formation is the matching of the electron and hole Fermi surfaces [20]. IXs being generated via laser excitation allows for the study of a charge neutral system that has an equal number of electrons and holes, this in turn means the Fermi momentum of electrons and holes are equal. As such, with sufficient cooling, the system can potentially form a BCS-like condensate.
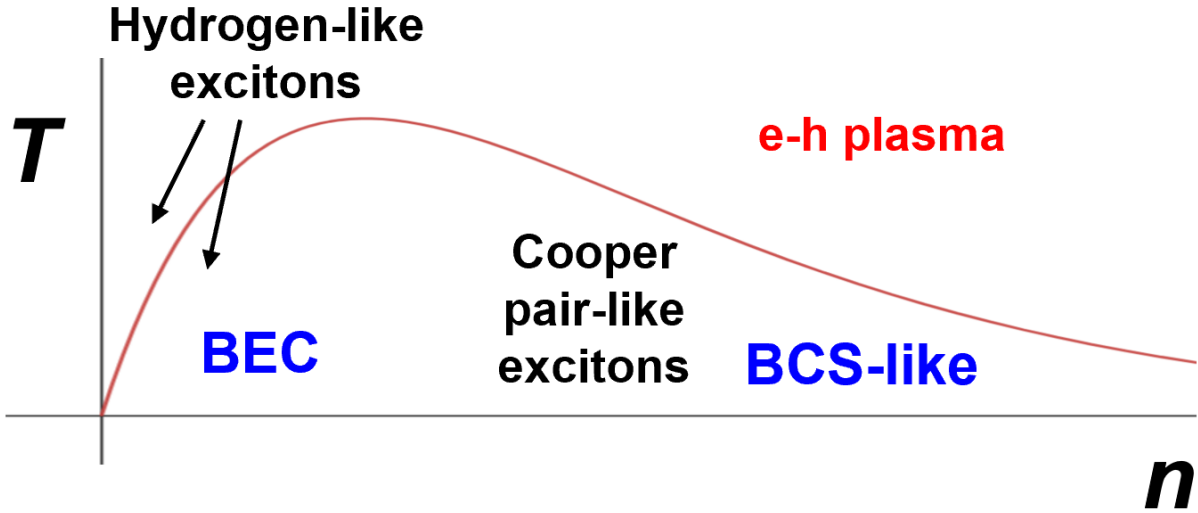
Figure 1.3: Phase diagram of ultracold e-h system. In the low density regime a BEC of hydrogen-like IX can form below the critical temperature. At high densities Cooper-pair-like excitons a BCS-like exciton condensate can form.

Dipolar Bosons

As dipoles, IXs allow for the study of dipolar boson interactions. When all dipole moments point the same direction the energy from this interaction, U_{dd}, is given by $U_{dd}(\boldsymbol{r}) = \frac{d^2}{\varepsilon}\frac{1-3\cos^2\theta}{r^3}$ where θ is the angle between the dipole direction and the relative position of the dipoles, d is the dipole moment, ε the dielectric constant, and r is the distance between dipoles. We see from this equation that typically IXs feel dipolar repulsion as they exist in the same plane of the CQW, however by creating a system with two sets of CQW a system can be constructed where some IXs feel dipolar attraction [8].

1.4: IXs in devices

The unique properties of IXs make them an interesting platform to construct devices that use excitons, rather than electrons. The ease of control of the potential landscape of an excitonic

device also makes it relatively easy to develop device designs. Previous research has shown optical excitonic transistors [26] [27], transistors [28] [29], and excitonic integrated circuits [30].

Optically active

Due to their radiative recombination, IXs can interface with optical communications systems directly. Additionally, the photons emitted retain information about momentum and spin of the IX.

Bosonic particles

Rather than fermionic particles communicating information in electronic devices, IX are bosons. As such a condensate of IX would require a much lower switching voltage for an excitonic transistor than a similar electronic device as a BEC would all be in the ground state, which is impossible in the electronic system due to Pauli exclusion.

Device scaling

The numerous properties of IX also allow for the construction of smaller devices compared to other systems. The exciton Bohr radius is typically 10nm in GaAs and 1nm or less in transition metal dichalcogenides (TMDs), and due to their ability to optically couple, this allows for the construction of optically active devices potentially at sub-photon wavelength scales (400~1000nm).

Existing devices and future work

Much work has already been done on excitonic devices; however, the exciton range of existence is limited by temperature where $k_B T \sim E_X$ where k_B is the Boltzmann constant and E_X is the exciton binding energy. Thermal energy disrupts the bound pair. In GaAs/AlAs CQWs excitonic devices have been seen to operate up to 100K [28]. In GaAs IX's binding energy has been observed up to ~10meV while TMDs have shown binding energies up to 350meV, allowing

for the existence of excitons at room temperature [31]. This provides a potential medium for room temperature IX devices.

1.5: Previous work

Before working on the projects described in chapters 3 and 4 I participated in two other projects. The first of which was on a wide single quantum well sample where I aided in measurements and sample fabrication. Typical experiments studying IXs involve separated layers of electrons and holes, however disorder in CQW is typically due to fluctuations on the QW widths, as the energy of a particle in QW with width L scales roughly as $1/L^2$ [9]. As such wide QWs will have less disorder. A wide single quantum well (WSQW) has been studied in IX systems, but no long range transport was demonstrated [32] [33]. Due to the quality of the sample studies by our group and quality of electrode fabrication we demonstrated high IX mobility, spectrally narrow IX emission, voltage-controllable IX energy, and long and voltage-controllable IX lifetime [9].

The second project involves a TMD heterostructure made from $MoSe_2/WSe_2$ where I aided in the construction of the assembly stage used to construct the sample.

1.6: Thesis outline

The experimental methods such as optical spectroscopy and electric field application used in subsequent chapters are described in chapter 2. The experimental results of attractive behavior between dipolar bosons are discussed in chapter 3 alongside comparisons with theory. Finally, chapter 4 describes the realization of a Fermi-edge singularity in a neutral electron-hole plasma, which evidences the formation of Cooper pair-like excitons at the Fermi edge, the first experimental results of Cooper pair-like excitons.

Chapter 2: Experimental Methods

2.1 Optical Spectroscopy

Due to the ability to create IXs via laser excitation and their photoluminescence upon decay, optical spectroscopy is a powerful way to study IXs. Excitons are first generated via laser excitation which excites electrons and holes and the energy landscape of the sample allows formation of spatially indirect excitons. The wavelength of the laser excitation is often controlled in these systems in order to maximize absorption or study the behavior with changing excitation wavelength. Laser(s) excitation is focused onto the sample via an objective lens, typical spot size FWHM is 3-10 µm. By varying how laser excitation is applied different exciton clouds can be formed. Two types of lasers were used in the works presented in chapters 3 and 4, in chapter 3 diode lasers, tuned to 1.532 and 1.541 eV, were used and a Titanium Sapphire laser (Ti Saph) was used in chapter 4. While the titanium sapphire laser has a tunable wavelength by changing the laser cavity, the diode laser's wavelength is primarily temperature dependent. As such we constructed temperature-controlled mounts using Peltier chips to control the wavelength of the diode laser. This resulted in control of the wavelength across a range of ~±5nm with accuracy within a quarter nm. Due to resonances in the laser system certain wavelengths would be preferred over others, which varies from diode to diode.

As an exciton decays it emits a photon, the exciton photoluminescence (PL) is then focused onto a spectrometer and nitrogen cooled charge coupled device camera (CCD) which allows for the spatially and spectrally resolved images of IX PL. To achieve temporal resolution, we utilized coupled pulse generators, one which controls the laser pulse emission and the second, slaved to the first, controls an intensified CCD's (ICCD) integration window and timing with respect to the laser pulse. While the diode lasers could be controlled by the pulse generators alone, the Ti Saph

needed to be sent through an acousto-optic modulator which would direct the beam down the beamline in time with the pulse. The combination of ICCD and pulsed laser allows pulsed excitation (typically on order of 1μs) and control of the temporal measurement window (typicallu on order of 50ns), allowing for the study of emission at any time during or after the laser pulse. An example of this set up, used in the measurements presented in Chapter 4, is shown in **Figure 2.1**. If measured while the laser is on, the expansion of the exciton cloud can be studied, while if measured with the laser off the decay of the exciton photoluminescence, as well as luminescence without contributions from laser excitation and bulk emission can be studied. One can use this to measure the lifetime of the IX in a system. Measuring after the pulse is also particularly useful as excitation resonant with the DX emission is often used to maximize IX created, and results in laser light very close spectrally to the IX emission. This can make it difficult to detect the IX PL when the exciting laser is on. Additionally, laser excitation can heat the exciton system, so by measuring after the laser has turned off there is sufficient time for the excited system to cool to the lattice temperature.
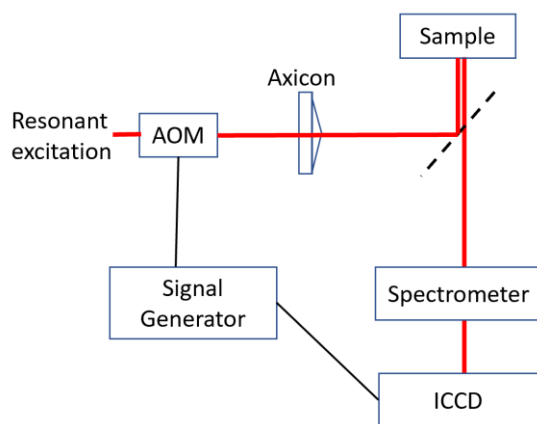
Figure 2.1: Schematic of optical excitation and collection used in Chapter 4. Resonant excitation from the Titanium Sapphire laser is fed into an AOM which is pulsed with a signal generator. The pulsed excitation is then sent through an axicon to shape the beam and focused onto the sample via an objective. The emission is then focused onto a spectrometer and then ICCD that is controlled by a signal generator. This allows for the coordination of the pulsed laser and timed emission collection.

2.2 Cryogenic measurements

Due to IX being limited by $k_B T \sim E_X$ all of the measurements here were performed in a helium vapor cryostat. This cryostat allows for the control of the temperature of the sample from 1.5-300K. Measurement temperatures in chapter 4 vary from 2-25K.

2.3 Coupled quantum wells

To form spatially indirect excitons a pair of coupled quantum wells (CQWs) is typically used. In GaAs samples this is formed from GaAs quantum wells separated by AlGaAs.

The CQWs in GaAs require an applied voltage for the formation of IX. To achieve this a platinum electrode is applied to the top of the sample while a Si doped n^+ GaAs backgate serves as a bottom ground electrode. The width of the GaAs wells determines the binding energy, lifetime, and dipole moment. This allows for a system with 2 CQW with different energies, described in chapter 3 [8]. The GaAs samples are grown via molecular beam epitaxy.

Chapter 3: Attractive and repulsive dipolar interaction in bilayers of indirect excitons

3.1 Introduction

A spatially indirect exciton (IX), also known as an interlayer exciton, is a bound pair of an electron and a hole confined in separated layers. Due to the electron-hole separation, IXs have built-in electric dipole moment ed, where d is the distance between the electron and the hole layers, and e is the electron charge. Furthermore, due to the electron-hole separation, IXs have long lifetimes within which they can cool below the temperature of quantum degeneracy [34]. These properties make IXs a platform for exploring quantum gases with dipolar interaction.

IXs can be realized in a pair of quantum wells separated by a narrow tunneling barrier. For one layer of IXs in a single pair of coupled quantum wells (CQWs), the out-of plane IX electric dipoles lead to repulsive dipolar interaction between side-to-side IX dipoles (Fig. 3.1). This configuration is extensively studied both theoretically and experimentally. The phenomena originating from the repulsive dipolar interaction in a single IX layer include the enhancement of IX energy with density that has been known since early studies of IXs [35] [14] [36] [37] [5], screening of the in-plane disorder potential by repulsively interacting IXs [21] [38] [39] [10] that leads to IX delocalization and long-range IX transport [21] [38] [39] [10] [11] [40] [41] [42] [43] [44] [45] [9], strong correlations, [10] [46] [47] [48] [49] [50] [51] [52] [53], and predicted crystal phases [54] [55] [56] [57] [58] [59] [60] [61].

Quantum gases with dipolar interaction are also explored with cold atoms. In these systems, dipolar interactions lead to droplet structures with spatial ordering and coherence [62] [63] [64] [65] [66], few-body complexes [67] [68], and a pair of superfluid and crystal phases in bilayers of dipoles [69] [70] [71] [72].

The specific property of dipolar interaction is its anisotropy. For instance, for two parallel dipoles tilted at angle θ relative to the line connecting them, the interaction at r>>d$_1$, d$_2$ is given by $v(r) \sim e^2 d_1 d_2 (1 - 3\cos^2\theta)/\epsilon r^3$, where ϵ is the dielectric constant of the material and p$_{1,2}$ = $ed_{1,2}$ are the dipole moments. For the out-of-plane IX dipoles in a single IX layer this expression reduces to $v(r) \sim e^2 d^2/\epsilon r^3$ describing the repulsive dipolar interaction between IXs.

The other specific property of dipolar interaction for the IXs is the induced orientation of IX dipoles. The heterostructure design and/or applied voltage, which produces the electric field in the heterostructure, determine the quantum well layers where electrons and holes are confined: Exchanging the quantum wells by the electron and the hole, i.e., flipping the IX dipole, is energetically unfavorable. Furthermore, tilting the IX dipole relative to the *z* direction causes an in-plane separation of the electron and the hole in the IX and, as a result, reduces the IX binding energy. This induces the orientation of IX dipoles in the direction normal to the QW plane.

The induced orientation of the IX dipoles and the repulsive dipolar interaction for a single IX layer makes it challenging to explore the attractive dipolar interaction in IX systems. The studies of IX dipoles have been concentrated on the case of repulsively interacting IXs [34]- [58]. However, the angle dependent dipolar IX interaction and, in particular, dipolar attraction give access to new phenomena in quantum dipolar gases. For instance, the dipolar attraction leads to the phenomena in cold atoms outlined above [62]- [72]. IX attraction can be realized by extending IX heterostructures beyond a single CQW design, and studies of attractively interacting IX dipoles were recently started in two stacked CQW pairs [73] [74] [75].

In this chapter, we explore the attractive dipolar interaction between IXs in a two-CQW heterostructure with two IX layers in two separated CQW pairs (Fig. 3.1). The intra-CQW interaction between IX side-to-side dipoles is repulsive similar to single CQW heterostructures

[34]- [58]. The inter-CQW interaction between IX head-to-tail dipoles is attractive. It changes to repulsive with increasing in-plane separation between the IXs and, in turn, θ following the anisotropy of dipolar interaction outlined above. Both our experimental measurements and our theoretical simulations show: (i) a monotonic energy reduction for IXs in one layer with increasing density of IXs in the other layer, and (ii) an in-plane shift of a cloud of IXs in one layer towards a cloud of IXs in the other layer. This behavior is qualitatively consistent with attractive dipolar interaction, however, the measured IX energy reduction and IX cloud shift are higher than the values given by the correlated liquid theory.

3.2 Experiment

The studied two-CQW heterostructure [Fig. 3.1(a)]is grown by molecular beam epitaxy. Indirect excitons IX_2 form in CQW_2, indirect excitons IX_1 form in CQW_1. CQW_2 consists of two 15-nm GaAs QWs separated by a 4-nm $Al_{0.33}Ga_{0.67}As$ barrier, CQW_1 consists of two 12-nm GaAs QWs separated by a 4-nm $Al_{0.33}Ga_{0.67}As$ barrier. CQW_2 and CQW_1 are separated by a 12-nm $Al_{0.33}Ga_{0.67}As$ barrier, narrow enough to allow substantial interlayer interaction between IX_2 and IX_1, yet wide enough to suppress tunneling of electrons and holes between CQW_2 and CQW_1. n^+-GaAs layer with $n_{Si} \sim 10^{18}$ cm^{-3} serves as a bottom electrode. The CQW pair is positioned 100 nm above the n^+-GaAs layer within the undoped 1-μm-thick $Al0_{.33}Ga_{0.67}As$ layer. The two CQW pairs are positioned closer to the homogeneous bottom electrode to suppress the fringing in-plane electric field in excitonic devices [76]. The top semitransparent electrode is fabricated by applying 2-nm Ti and 7-nm Pt on a 7.5-nm GaAs cap layer. Applied gate voltage $V_g =-2$ V creates an electric field in the z direction. The cross section of the heterostructure is presented in section 3.5.5.
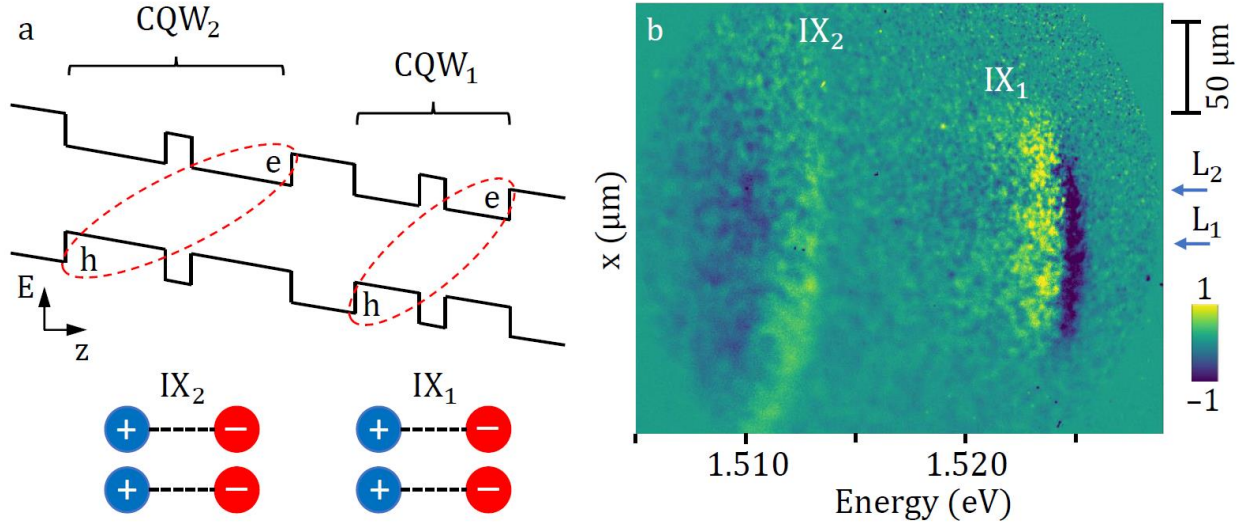
Figure 3.1: Two-CQW heterostructure and x-energy image. (a) Diagram of the two-CQW structure with two CQW pairs. IX_2 forms in CQW_2, and IX_1 forms in CQW1. Schematic below shows IX dipoles. $-$ electrons and $+$ holes. The intra-CQW interaction between IX_2 (or IX_1) side-to-side dipoles is repulsive. The inter-CQW interaction between IX_2 and IX_1 head-to-tail dipoles is attractive. (b) Differential x-energy luminescence image. The arrows indicate the excitation spot positions of the L_2 and L_1 lasers resonant to direct excitons in 15-nm CQW_2 and 12-nm CQW_1, respectively. L_2 generates IX_2. L_1 generates IX_1 and a smaller concentration of IX_2. The laser powers $PL_1 = 10\ \mu W$, $PL_2 = 250\ \mu W$. The differential x-energy image is obtained by subtracting the x-energy images created by only L_1 on and by only L_2 on from the x-energy image created by both lasers on. In the differential x-energy image, the yellow and blue colors indicate the enhancement and reduction of the IX luminescence intensity, respectively. For the energy axis, the blue region on the right side and the yellow region on the left (observed for IX_1) correspond to an energy decrease. For the position axis, the blue region on the low side and the yellow region on the high side (observed for IX_1) correspond to a cloud shift up. The differential x-energy image shows an increase in IX_2 energy, a decrease in IX_1 energy, and a spatial shift of the IX_1 cloud towards the IX_2 cloud.

The IX_2 energy is lower than the IX_1 energy. This energy difference gives an opportunity to selectively generate IX_2 by optical excitation. Excitons are generated by semiconductor lasers L_2 and L_1 at the energies 1.532 and 1.541 eV resonant to spatially direct excitons (DXs) in CQW_2 and CQW_1, respectively. The resonant to DX excitation increases the light absorption and, in turn, IX density for a given laser power [77]. L_2 generates IX_2. L_1 generates IX_1 and roughly a two times smaller concentration of IX_2 due to a weaker non resonant absorption of L_1 light in CQW_2. L_2 and L_1 excitations are focused to $\sim$5-μm half width at half maximum spots, which are separated by 50

µm. This configuration allows exploring the effects of IX interactions on the IX cloud position. IX photoluminescence (PL) is measured in a 20-ns time window starting 20 ns after the end of the L_1 and/or L_2 excitation pulses. This allows for studying of only long-lived IXs after DXs recombined. Both IX_2 and IX_1 have long lifetimes in the range of hundreds of nanoseconds ($\sim$800 ns for IX_2 and $\sim$260 ns for IX_1) allowing them to travel over long distances reaching hundreds of microns.

Time-resolved imaging experiments are performed with a laser pulse duration 2000 ns, period 4000 ns, and edge sharpness $\sim$2 ns. The rectangular-shaped pulses are realized by a pulse generator driving the semiconductor lasers. The pulse duration and period are optimized to allow the IX PL image to approach equilibrium during the laser excitation and decay between laser pulses. The PL images are captured using a PicoStar HR TauTec time-gated intensifier. The PL passes through a spectrometer with a resolution of 0.18 meV before entering the intensifier coupled to a liquid nitrogen-cooled CCD. The measurements are performed at $T_{bath} = 1.7K$.

To analyze the attractive interlayer IX interaction in the IX bilayer we measure how the selective generation of IX_2 affects the energies and cloud position of IX_1. Figure 3.1 (b) presents the differential x-energy image obtained by subtracting the x-energy images created by only L_1 on [Fig. 3.10(c) in section 3.7] and by only L_2 on [Fig. 3.10(b)] from the x-energy image created by both lasers on simultaneously [Fig. 3.10(a)]. The differential x-energy image shows an increase in IX_2 energy, a decrease in IX_1 energy, and a spatial shift of the IX_1 cloud towards the IX_2 cloud. These phenomena are detailed below.
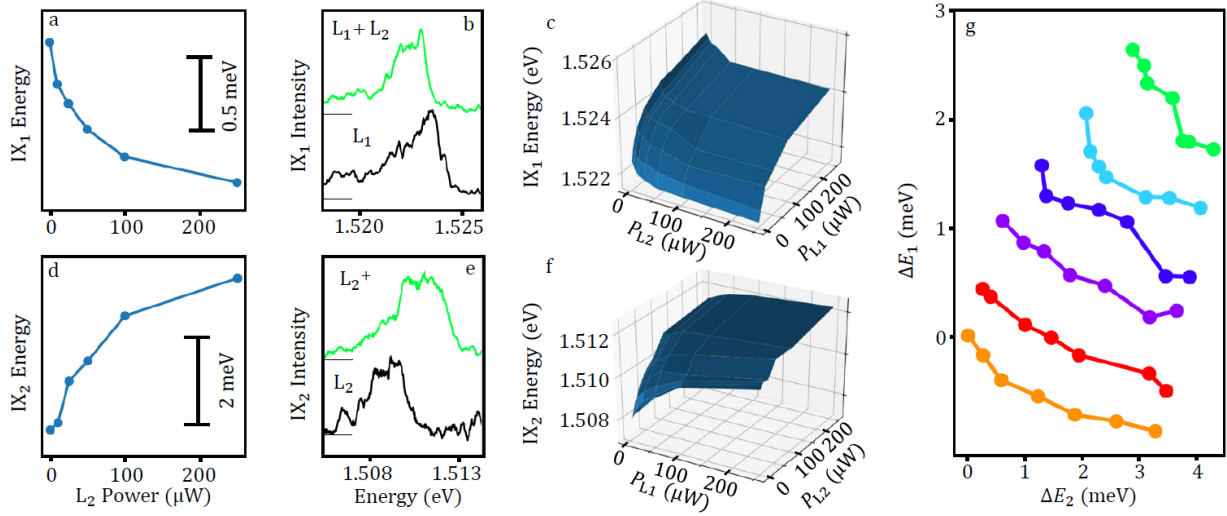
Figure 3.2: Decrease and increase of IX energy due to attractive and repulsive dipolar IX interactions: Experiment. (a) The decrease in IX_1 energy with increasing L_2 power and, in turn, IX_2 density. $P_{L1} = 10$ μW. An energy decrease corresponds to attractive IX_1-IX_2 interaction. (b) The redshift of the IX_1 spectrum with turning on L_2, which increases IX_2 density. The black line shows the IX_1 spectrum when only L_1 is on, $P_{L1} = 10$ μW. The green line shows the IX_1 spectrum when an additional L_2 is on, $P_{L2} = 250$ μW. (c) IX_1 energy as a function of both P_{L1} and P_{L2}. (d) The increase in IX_2 energy with increasing L_2 power and, in turn, IX_2 density. $P_{L1} = 0$. An energy increase corresponds to repulsive IX_1-IX_2 interaction. (e) The blueshift of the IX_2 spectrum with increasing L_2 power, which increases IX_2 density. $PL_2 = 25$ μW (black line) and 250 μW (green line). (f) IX_2 energy as a function of both P_{L1} and P_{L2}. (g) The change in IX_1 energy vs the change in IX_2 energy. Each set of data corresponds to increasing L_2 power. For the sets of data presented by orange, red, purple, blue, cyan, and green points, $L_1 = 5,10,25,50,100$, and 250 μW, respectively.

First, we consider the IX energy variations. Figures 3.2(a)-2(c) show that the increase in L_2 power (P_{L2}) and, in turn, IX_2 density (n_2) leads to a monotonic decrease in IX_1 energy. An energy decrease corresponds to attractive IX_1-IX_2 interaction. In comparison, when only IX_2's are present in the system (L_1 is off), the increase in P_{L2} and, in turn, n_2 leads to a monotonic increase in IX_2 energy [Figs. 3.2(d)–2(f)]. An energy increase corresponds to repulsive IX_2-IX_2 interaction, which has been extensively studied in single layers of IXs [34]- [58].

Figures 3.2(c) and 3.2(f) also show that the increase in P_{L1} leads to a monotonic increase in both IX_1 and IX_2 energies. L_1 generates both IX_1 and IX_2, therefore, the effect of increasing P_{L1}

on IX_1 (or IX_2) energy is a combined effect of attractive IX_1-IX_2 and repulsive IX_1-IX_1 (or IX_2-IX_2) interactions. The monotonic increase in both IX_1 and IX_2 energies with P_{L1} indicates that the repulsive interaction is stronger. This is consistent with the relative strength of the attractive [Fig. 3.2(a)] and repulsive [Fig. 3.2(d)] interaction in the experiments with increasing P_{L2} which increases only IX_2 density.
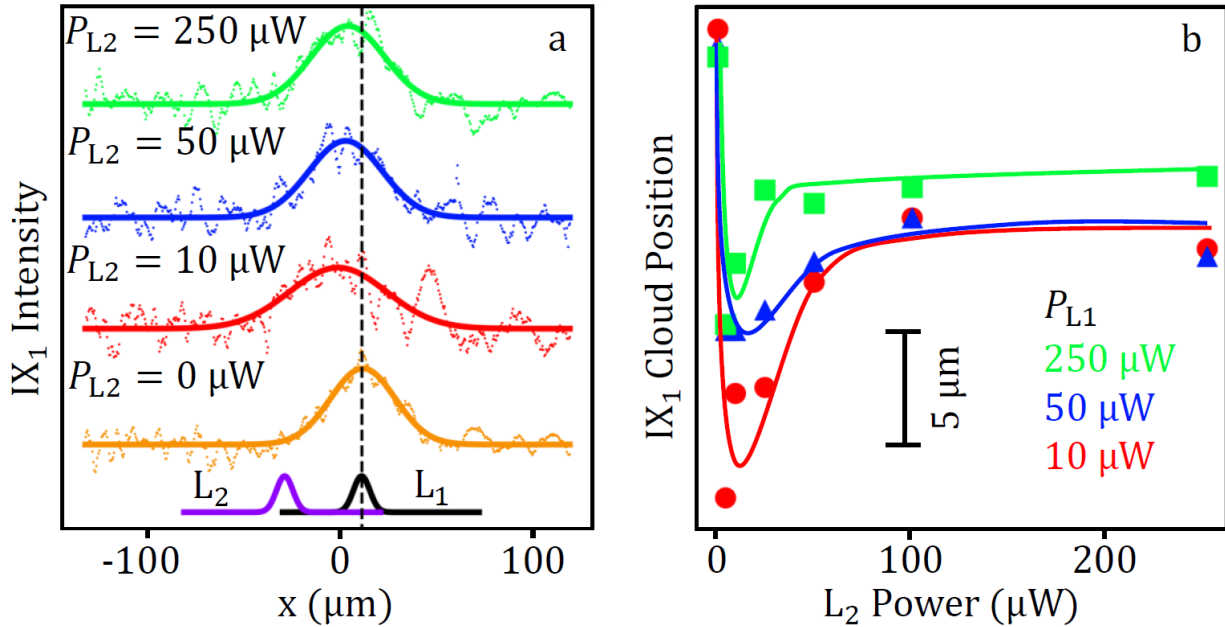
Figure 3.3: Attraction of the IX_1 cloud to the IX_2 cloud: Experiment. (a) The IX_1 cloud profiles at different P_{L2}'s and, in turn, IX_2 densities. P_{L1} = 10 μW. The profiles of the L_1 and L_2 laser excitation spots are shown by black and purple lines, respectively. The dashed line indicates the center of the L_1 excitation spot. (b) The center-of-mass position of the IX_1 cloud as a function of P_{L2} for different P_{L1}'s.

In the mean-field approximation the repulsive interaction between IXs in a single layer increases the IX energy by $\Delta E = 4\pi e^2 dn/\epsilon$. This equation known as the "plate capacitor" formula provides a qualitative explanation for the observed monotonic increase in ΔE with the exciton density n [35]. However, the capacitor formula can significantly overestimate $\Delta E(n)$ due to the IX correlations [10] [46] [47] [48] [49] [50] [51] [52] [53]. To compare the attractive and repulsive

dipolar interactions, avoiding the complexity of the relation between E and n, Fig. 3.2(g) presents the change in IX_1 energy E_1 vs the change in IX_2 energy E_2 for the data in Figs. 3.2(c) and 3.2(f).The energy shifts E are measured relative to the IX energies at the lowest n. Figure 3.2(g) shows that for all studied P_{L1}'s, the increase in P_{L2} and, in turn, n_2 leads to E_2 larger in absolute value than E_1, indicating that the repulsive IX_2-IX_2 interaction is stronger than the attractive IX_2-IX_1 interaction.

We also consider the spatial shift of the IX_1 cloud toward the IX_2 cloud. Figure 3.3 shows that the IX_1 cloud attracts to the IX_2 cloud. With increasing PL_2, the spatial shift is nonmonotonic. This behavior is observed for different PL_1's. A larger spatial shift, reaching ~ 10 μm, is observed at low P_{L1} [Fig. 3.3(b)].

3.3 Theory

We analyze the dipolar interaction in IX bilayers theoretically and compare the experimental data with theoretical simulations. The numerical simulation of a such two-species many-body system is performed through the hypernetted chain (HNC) formalism [78]. The intra- and interlayer interactions are modeled by assuming that the wave function of electrons and holes are isotropic Gaussians and they experience a Coulomb interaction, see section 3.5. The HNC method has been previously used for studying bosons with dipolar interactions in single-layer systems [79]. Unless the interaction strength is very high, the HNC predictions for basic many-body properties, such as pair-correlation functions and energy per particle were shown to be in good agreement with the more accurate Monte Carlo calculations [56] [71] [72].
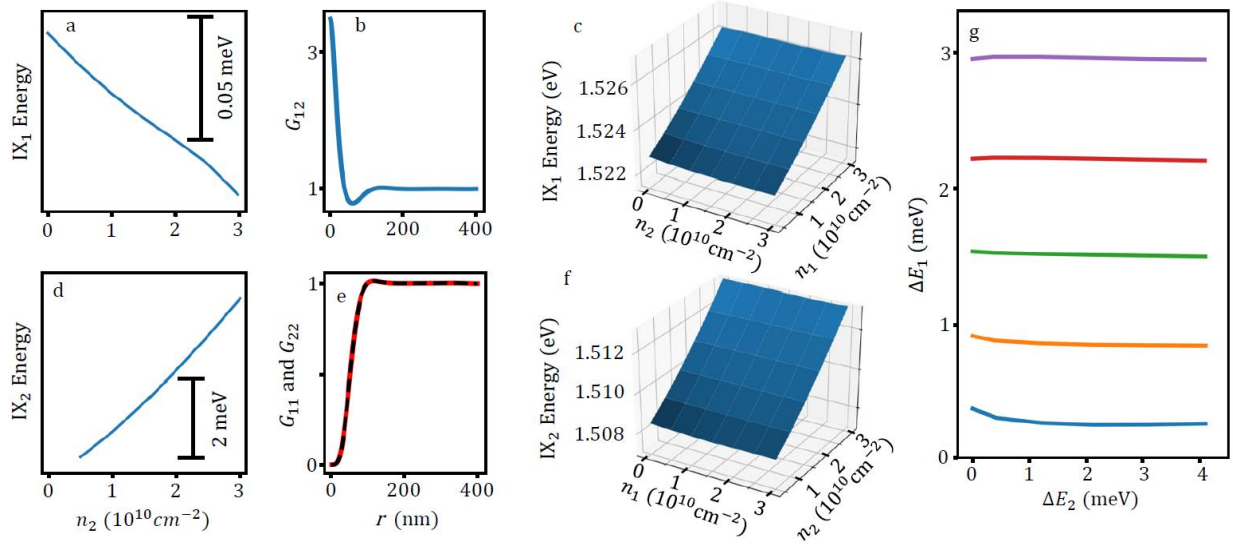
Figure 3.4: Decrease and increase in IX energy due to attractive and repulsive dipolar IX interactions: Theory. (a) The decrease in IX_1 energy with increasing IX_2 density. $n_1 = 1.5 \times 10^{10}$ cm^{-2}. An energy decrease corresponds to attractive IX_2-IX_1 interaction. (b) IX_1-IX_2 density correlation function. $n_1 = n_2 = 10^{10}$ cm^{-2}. (c) IX_1 energy as a function of both IX_1 and IX_2 densities. (d) The increase in IX_2 energy with increasing IX_2 density. $n_1 = 0$. An energy increase corresponds to repulsive IX_2-IX_2 interaction. (e) IX_2-IX_2 (red solid line) and IX_1-IX_1 (black dashed line) density correlation functions. $n_1 = n_2 = 10^{10}$ cm^{-2}. (f) IX_2 energy as a function of both IX_1 and IX_2 densities. (g) The change in IX_1 energy vs the change in IX_2 energy. Each line corresponds to increasing IX_2 density. For the blue, orange, green, red, and purple lines, $n_1 = 0.5, 1, 1.5, 2$, and 2.5×10^{10} cm^{-2}, respectively.

The simulated IX energy shifts caused by the attractive and repulsive IX dipolar interactions are presented in Fig. 3.4. Figures 3.4(a) and 3.4(c) show that the increase in n_2 leads to a monotonic decrease in IX_1 energy due to the attractive IX_1-IX_2 interaction, in qualitative agreement with the experimental data in Figs. 3.2(a) and 3.2(c). In contrast, the increase in n_2 (or n_1) leads to a monotonic increase in IX_2 (or IX_1) energy [Figs. 3(d) and 3(f)] due to the repulsive IX_2-IX_2 (or IX_1-IX_1) interaction, in qualitative agreement with the experimental data in Figs. 3.2(d) and 3.2(f).

In the simulations, n_1 is increased selectively keeping n_2 intact. In the experiment, an increase in n_1 is accompanied by an increase in n_2 as outlined above. This leads to different

variations of IX$_2$ energy with n_1 in the experiment [Fig. 3.2(f)] and the theory [Fig. 3.4(f)]. However, the conclusions on the attractive IX$_1$-IX$_2$ interaction and repulsive IX$_2$-IX$_2$ interaction derived from the experiment and the comparison between the experiment and the theory are based on the n_2 dependence and are not affected by the difference in the n_1 dependence.

The density correlation functions for the cases of attractive IX$_1$-IX$_2$ and repulsive IX$_1$-IX$_1$ and IX$_2$-IX$_2$ interactions are presented in Figs. 3.4(b) and 3.4(e), respectively. For the attractively interacting IXs [Fig. 3.4(b)], the correlation function enhancement above 1, the mean-field value, increases the interaction energy compared with the vanishing interlayer interaction in the mean-field approximation. On the contrary, the repulsively interacting IXs avoid each other [Fig. 3.4(e)] that lowers the intralayer IX interaction energy compared with the uncorrelated state assumed in the mean-field approximation.

The energy shift in Fig. 3.4(d) is close to 1/3 of the shift given by the plate capacitor formula, in other words, the exciton density is related to the measured energy shift caused by the intralayer IX interaction by the formula $\Delta E = 1/3 \times 4\pi e^2 dn/\epsilon$. In Figs. 3.2(d) and 3.4(d), the ranges of the energy shift in the experiment and the theory are similar so that the range of the L$_2$ laser power in Fig. 3.2(d) approximately corresponds to the range of the exciton density n_2 in Fig. 3.4(d).

As for the experimental data, we compare the attractive and repulsive dipolar interactions in a graph showing E_1 vs E_2. Figure 3.4(g) shows that for all studied n_1, the increase in n_2 leads to calculated E_2 larger in absolute value than E_1, in qualitative agreement with the experimental data in Fig. 3.2(g).
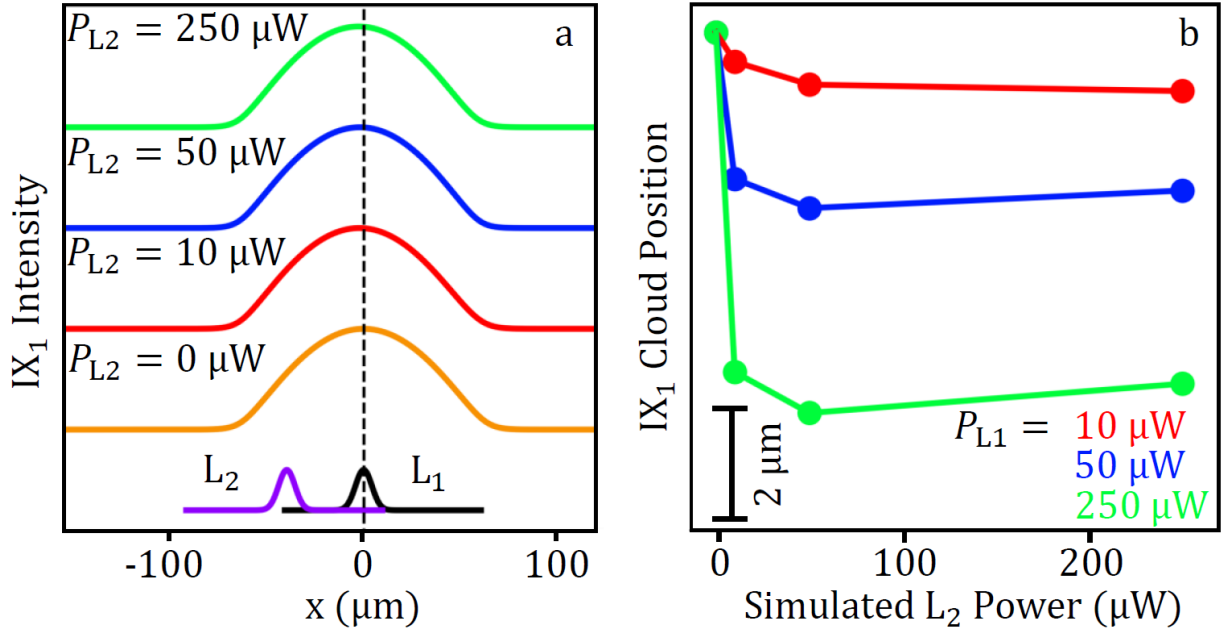
Figure 3.5: Attraction of the IX_1 cloud to the IX_2 cloud: Theory. (a) The IX_1 cloud profiles simulated for different P_{L2}'s and, in turn, IX_2 densities. $P_{L1} = 250$ μW. The profiles of the L_1 and L_2 laser excitation spots are shown by black and purple lines, respectively. The dashed line indicates the center of the L_1 excitation spot. (b) The center-of-mass position of the IX_1 cloud as a function of P_{L2} for different P_{L1}'s.

We also simulated the spatial shifts of the IX_1 cloud toward the IX_2 cloud. The simulations of the IX spatial profiles are based on the IX generation, diffusion, and recombination and are outlined in section 3.5.3. Figure 3.5 shows that the IX_1 cloud attracts to the IX_2 cloud in the simulations, in qualitative agreement with the attraction observed in the experiment (Fig. 3.3). In comparison, both our experimental measurements (Fig. 3.8) and theoretical simulations (Fig. 3.9) show that two clouds of repulsively interacting IX_2 repel each other, see section 3.6.

Although both the experimental measurements and the theoretical simulation show: (i) a monotonic IX_1 energy reduction with increasing IX_2 density, and (ii) an in-plane shift of IX_1 cloud towards the IX_2 cloud, consistent with attractive dipolar interaction, the measured IX_1 energy reduction and IX_1 cloud shift are higher than the values given by the correlated liquid theory [compare Fig. 3.2(a) with Fig. 3.4(a),Fig. 3.2(g) with Fig. 3.4(g), and Fig. 3.3 with Fig. 3.5]. The

interaction- and/or disorder-induced IX mass enhancement may be one possible reason for this discrepancy. The magnitude of IX_1 energy reduction E_1 scales with the strength of interlayer IX_1-IX_2 dipolar attraction (Fig. 3.6). For the case of a single pair, E_1 can be estimated as the binding energy of IX_1-IX_2 biexciton state E_b. For a bare IX mass $m_{IX} \sim 0.2\ m_0$ [80], $E_b \sim 0.3$ meV (Fig. 3.7). Higher E_b can be achieved for higher IX masses, and, e.g., for the reduced IX mass enhanced to 2 m_0, E_b reaches ~ 1.2 meV (Fig. 3.7), making the IX_1-IX_2 interaction scale comparable to the experiment (Fig. 3.2). A mass enhancement can be caused by interaction, however, only a relatively weak interaction-induced mass enhancement, up to $\sim 25\%$, was observed in electron-hole systems in single QWs [81]. The studies of effects of interaction and/or disorder on the IX mass can be a subject of future work.
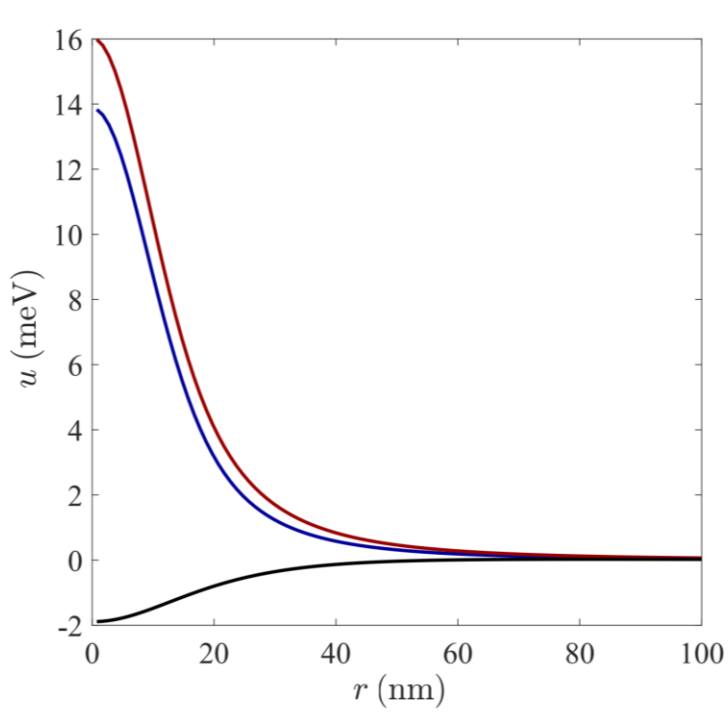

Figure 3.6: Model interaction potentials: u_{22} (top) and u_{11} (middle) are the intra-CQW potentials for IX_2 and IX_1, respectively; u_{12} (bottom curve) is the inter-CQW interaction potential. Parameters: $d_1 = 20$, $d_2 = 25$, $D = 43$, $a = 5$ (all in nanometers); $\epsilon = 13$.

Layered heterostructures with more than one IX layer, such as IX bilayers in this paper, and, generally, with more than two electron and hole layers, such as three-layer heterostructures in Ref. [82], could be new platforms for studying systems with attractive dipolar interaction. For heterostructures with a fixed set of materials, the range of parameter variation may be limited. For instance, for the GaAs/AlGaAs heterostructures used in this paper, it is difficult to achieve a significant change in the dipolar attraction between the IXs by varying the AlGaAs spacer layer thickness d_s: A significant reduction of d_s would lead to substantial tunneling of electrons and holes between CQW_1 and CQW_2, destroying both IX_1 and IX_2, whereas a significant enhancement of d_s would lead to a substantial reduction of the dipolar interaction, which drops as $1/r^3$ and is already weak for $d_s = 12$ nm in the heterostructure studied in this paper.
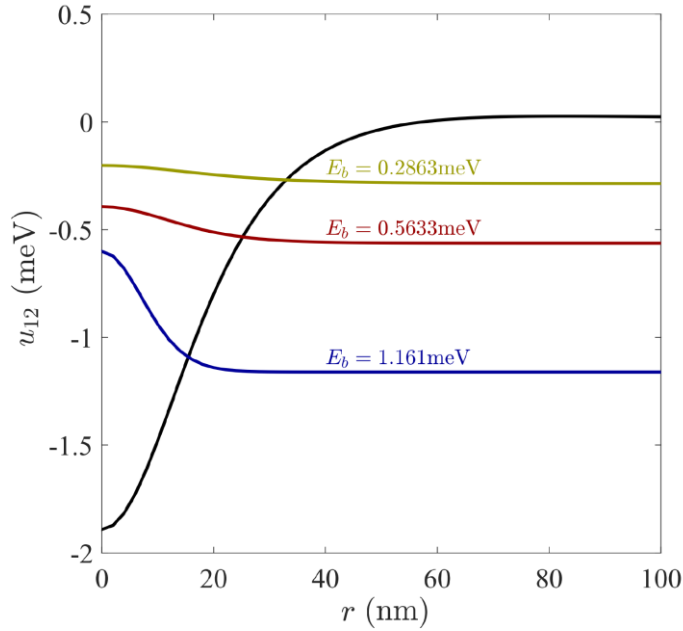
Figure 3.7: Probability density distributions of inter-CQW biexcitons within the rigid-body approximation. The interaction potential u_{12} (the same as in Fig. 3.6) is shown by the curve with a dip (black curve). The probability distributions (wave functions squared) of the bound states are depicted by the curves with the maxima. These curves are plotted in arbitrary units and are offset to show the binding energies E_b. They correspond (top to bottom) to the reduced masses of 0.5, 1, and 10 of the exciton mass.

However, a significant change in the parameters can be achieved by using different materials. In particular, van der Waals heterostructures offer an opportunity to study IX bilayers with small d and/or d_s (significantly smaller than in the GaAs heterostructures) and high IX binding energies (significantly higher than in the GaAs heterostructures), see Ref. [83] and references therein. The studies of dipolar interactions in IX bilayers and other IX systems with multiple electron and hole layers in van der Waals heterostructures can be a subject of future work.

3.4 Conclusion

To summarize, we presented experimental and theoretical studies of attractive dipolar interaction in IX bilayers. We found that increasing density of IXs in one layer causes a monotonic energy reduction for IXs in the other layer. We also found an in-plane shift of a cloud of IXs in one layer towards a cloud of IXs in the other layer. This behavior is qualitatively consistent with attractive dipolar interaction. The measured IX energy reduction and IX cloud shift are higher than the values given by the correlated liquid theory.

3.5 Supplemental Information

3.5.1 Interaction Potentials

We modeled IXs as composite bosonic particles with a rigid internal charge distribution. The interactions of such particles can be specified in terms of potentials $u_{ij}(r)$, $1 \leqslant i, j \leqslant 2$, which are functions of pairwise in-plane distances r of the excitons. We use subscripts 1 and 2 to label the CQWs (12-nm and 15-nm wide, respectively). To compute these interaction potentials, we assumed that the charge distributions of all the electrons and holes are spherically symmetric

Gaussians. The radius a of the Gaussians is our adjustable parameter that accounts for the width of the quantum wells and the internal motion of particles about the center of mass of each exciton. We computed these interaction potentials by taking the convolutions of the Coulomb kernel $e^2/\epsilon\sqrt[2]{r^2+z^2}$ with the charge densities of the interacting particle pairs. The result for the inter-CQW potential $u_{12}(r) = u_{21}(r)$ is

$$u_{12}(r) = \sum_{\sigma=\pm}\sum_{\tau=\pm} V(\sqrt{r^2+z_{\sigma\tau}^2}), \qquad (A1)$$

$$V(r) = \frac{e^2}{\epsilon r}\operatorname{erf}\left(\frac{r}{2a}\right), \qquad (A2)$$

$$z_{\sigma\tau} = \tau\frac{d_1-\sigma d_2}{2} + D, \qquad (A3)$$

where erf(x) is the error function and D is the z-axis distance between the CQW centers. The intra-CQW potentials $u_{kk}(r)$, $k = 1$, or 2, are given by the same equation with $D = 0$ and the electron-hole separations d_1 and d_2 replaced by d_k. The plots of these potentials for parameter values representative of our experimental device are shown in Fig. 3.6. At $r << a$ all of them approach constant finite values, and at large r, these potentials behave as $1/r^3$. Potentials $u_{11}(r)$ and $u_{22}(r)$ are strictly repulsive. The potential $u_{12}(r)$ is attractive in the range of distances r selected for the plot. At larger r, it eventually becomes repulsive, but it is already very small at such r.

The potentials $u_{ij}(r)$ serve as inputs to our computer program that computes many-body properties within the zero temperature HNC formalism. Another input parameter is the effective-mass m_{IX} of the excitons, which we took to be 0.2 of the free-electron mass m_0. Our implementation of the HNC method is based on Ref. [78]. The output of these calculations include the pair-correlation functions $G_{ij}(r)$, the energy density $\varepsilon = \varepsilon(n_1,n_2)$, and the chemical potentials,

$$\mu_j = \partial\varepsilon/\partial n_j, \qquad (A4)$$

of the excitons as functions of their number densities n_1 and n_2 in the CQWs. If the shake-up effects, i.e., many-body relaxation processes following the exciton recombination, can be

neglected, then the exciton emission energies (or exciton "single-particle energies") E_j should coincide with their chemical potentials,

$$E_j \approx \mu_j. \qquad (A5)$$

Based on this assumption, we have constructed the plot of ΔE_1 vs ΔE_2 shown in Fig. 3.4(g) of the main text. Representative intra-CQW and inter-CQW pair-correlation functions are plotted in Figs. 3.4(b) and 3.4(e). At short distances, these functions show a deep "correlation hole" for excitons of the same CQW and a strong correlation peak for excitons of different CQWs.

3.5.2 Biexciton binding energy

From previous theoretical work on double-layer bosonic systems with repulsive intralayer and attractive interlayer dipolar interactions [69] [70] [71] [72], we expect that the exciton system at low enough equal densities $n_1 = n_2$ should be made of bound pairs, the inter-CQW biexcitons. If $n_1 \neq n_2$, then biexcitons and unpaired excitons may coexist. A rough estimate of the required density is given by the Mott criterion stating that the biexcitons should appear when the dimensionless parameter $\min(n_1, n_2)b^2$ is less than some critical number, which is usually numerically small, perhaps, 0.02. Here b is the spatial size of the biexciton. Within our rigid-body approximation, the biexciton bound state can be easily found numerically. In the relative coordinates, this problem reduces to solving a Schrödinger equation for a particle of reduced mass $m_{IX}/2$ subject to the confining potential $u_{12}(r)$. For the same parameters as in Fig. 3.6, we obtained the binding energy to be $E_b = 0.286$ meV. From Fig. 3.7 we deduce the spatial size of the biexciton to be $b \sim 30$ nm so that the Mott critical density for biexcitons is on the order of 10^{10} cm^{-2}, not too far from the exciton densities realized in our experiment.
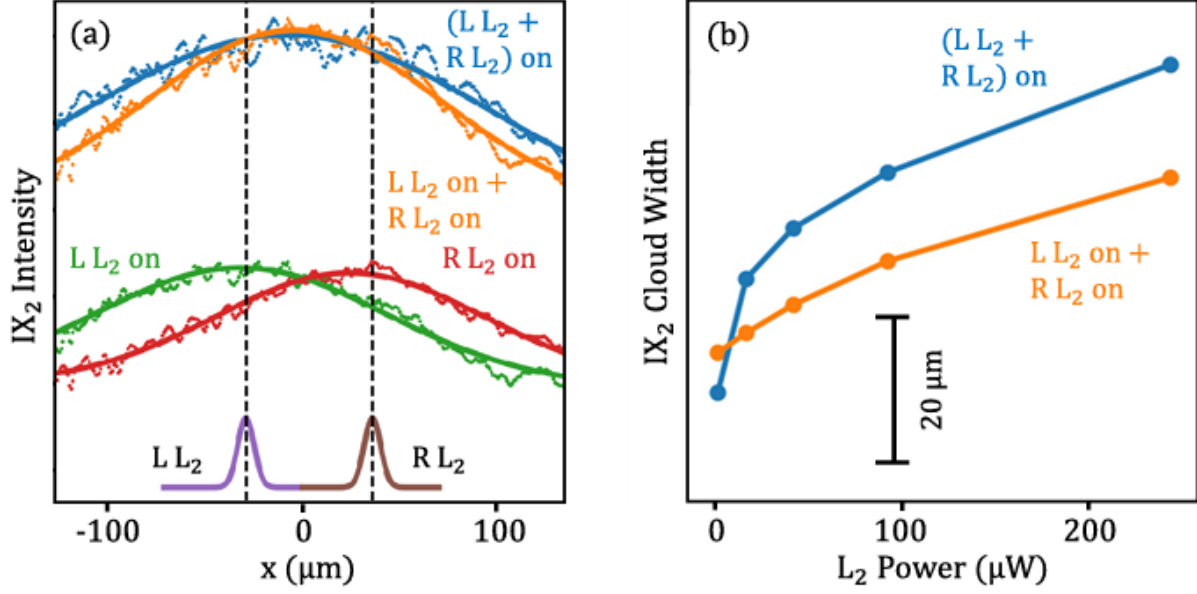
Figure 3.8: Repulsion between the IX_2 clouds: Experiment. (a) The IX_2 cloud profiles when only the left L_2 is on (L L_2 on, green line), when only the right L_2 is on (R L_2 on, red line), and when both left and right L_2's are on [(L L_2 + R L_2) on, blue line]. The sum of L L_2 on profile and R L_2 on profile (L L_2 on + R L_2 on) is shown by the orange line. Profile (L L_2 + R, L_2) on is wider than the sum of L, L_2 on profile and R, L_2 on profile, indicating the repulsion between the IX_2 clouds. The profiles of the left and right L_2 laser excitation spots are shown by purple and brown lines, respectively. The dashed lines indicate the centers of the excitation spots. (b) The width of the IX_2 cloud when both left and right L_2's are on [(L L_2 + R L_2) on, blue points] in comparison to the width of the IX_2 cloud obtained as the sum of L L_2 on the cloud and R L_2 on the cloud [L L_2 on + R L_2 on, orange points] as a function of P_{L2}.

The following argument suggests that E_b is, in fact, the maximum possible shift of the single-particle energies due to the inter-CQW attraction. Indeed, in the limit of high densities where average intra-CQW exciton separation is smaller than D, correlations are negligible. At intermediate densities where HNC should be accurate, the dependence of, say, $E_1 = E_1(n_1, n_2)$ on n_2 with n_1 held fixed is either monotonic or flat within computational accuracy, see Figs. 3.4(c) and 3.4(f). Therefore, the asymptotic limit $n_1 = n_2 \to 0$ where all excitons are paired and

$$E_1 = E_2 = -E_b \qquad (A6)$$

should correspond to the largest possible attraction effect. Note that the HNC method reproduces this asymptotic limit only approximately. The tendency toward pairing is manifested in the

aforementioned peak in the pair-correlation function $G_{12}(r)$ at $r = 0$. The shape of this peak computed by the HNC resembles the probability distribution of the biexciton, cf. Figs. 3.4(b) and 3.7. The integrated weight $N = n_2 \int G_{12}(r)d^2r$ of the peak (where the integration extends up to $r \sim b$) is the average number of excitons of CQW_1 attracted to an exciton in CQW_2. When the biexcitons form, N should approach unity. Yet within our HNC calculations N keeps increasing as $n_1 = n_2$ decreases. This suggests that the standard HNC method is inadequate in the low-density regime where we should instead use Eq. (A6).
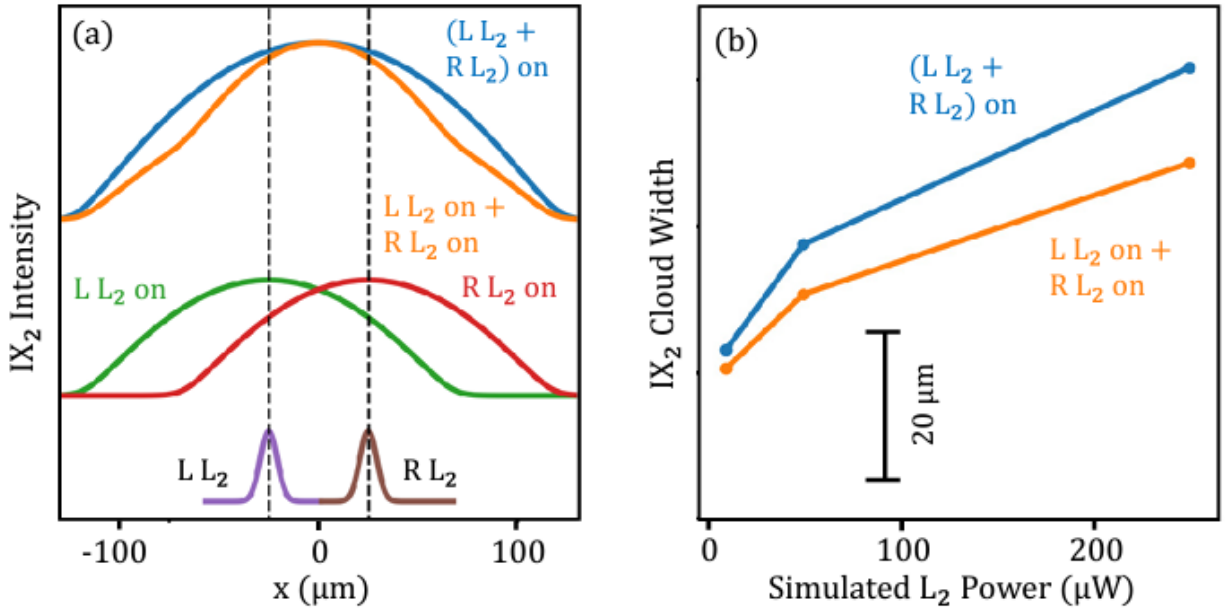

Figure 3.9: Repulsion between the IX_2 clouds: Theory. (a) The IX_2 cloud profiles simulated when only the left L_2 is on (L L_2 on, green line), when only the right L_2 is on (R L_2 on, red line), and when both left and right L_2's are on [(L L_2 + R L_2) on, blue line]. The sum of simulated L L_2 on profile and R L_2 on profile (L L_2 on + R L_2 on) is shown by the orange line. The profile (L L_2 + R L_2) on is wider than the sum of L L_2 on the profile and R L_2 on the profile, indicating the repulsion between the IX_2 clouds. The profiles of the left and right L_2 laser excitation spots are shown by purple and brown lines, respectively. The dashed lines indicate the centers of the excitation spots. (b) The width of the simulated IX_2 cloud when both left and right L_2's are on [(L L_2 + R L_2) on, blue points] in comparison to the width of the IX_2 cloud obtained as the sum of simulated L L_2 on the cloud and R L_2 on the cloud [L L_2 on + R L_2 on, orange points] as a function of P_{L2}.

We found both in experimental measurements [Fig. 2(a) and 2(c)] and theoretical simulations [Figs. 3.4(a) and 3.4(c)] that increasing density of IXs in one layer causes a monotonic energy reduction for IXs in the other layer. These results differ with the results of Refs. [74] [75] where a nonmonotonic dependence on the density was reported. The nonmonotonic dependence on the density was attributed to many-body polaron effects in Refs. [74] [75]. Our simulations show no indication for the nonmonotonic dependence on the density.

The experiment still poses a challenge for the theory because the shift of E_1 has been observed to routinely exceed the computed $E_b = 0.286$ meV, see Fig. 3.2(a). To identify a possible reason for the discrepancy, we examined this important parameter more critically. First, we tested the validity of the rigid-body approximation. We used a previously developed computational tool [60] to accurately solve for the exciton and biexciton binding energies as two-body and four-body problems, respectively. For the parameters of Fig. 3.6 we obtained $E_b = 0.33$ meV. Hence, the rigid-body approximation is not the major source of the discrepancy. Next, we noted that E_b is greatly reduced compared to the depth ≈ 2 meV of the potential well $u_{12}(r)$. This reduction is due to the zero-point motion. As an illustration of how this quantum effect may affect the binding energy, we recalculated E_b and the wave functions of biexcitons for reduced masses enhanced two- and 20-fold. In the latter case, the binding energy rises to 1.16 meV, see Fig. 3.7, which is close to the experimentally measured shifts of E_1 we attributed to the inter-CQW attraction. It is hard to expect that the exciton mass is indeed enhanced by such an enormous factor due to the interaction alone. (As a point of reference, only a relatively weak interaction-induced mass enhancement, up to 25%, was observed in electron-hole systems in single QWs [81].) However, the suppression of the zero-point motion of an exciton pair may, in principle, be facilitated by disorder in the system that traps the excitons close together in deep potential wells.

32

3.5.3 Dynamics of Exciton Density Distribution

In this section we summarize the set of equations we used to model the macroscopic dynamics of excitons. To simplify the modeling, we assumed that the exciton densities n_k and currents j_k were functions of a single spatial coordinate x. These quantities obey the continuity equation,

$$\partial_t n_k(x,t) = \partial_x j_k + g_k(x,t) - n_k \tau_k, \qquad (\text{B1})$$

where τ_k is the lifetime of the excitons in the kth CQW, which is known from the experiment, and g_k is the generation rate proportional to the local laser power. To represent the exciton currents, we used the drift-diffusion approximation,

$$j_k(x,t) = -D_k \partial_x n_k(x,t) - B_k n_k(x,t) \partial_x \mu_k \qquad (\text{B2})$$

where D_k and $B_k = D_k/T$ are the diffusion coefficient and the drift mobility, respectively. Finally, to simplify the treatment of interaction effects, we linearized the density dependence of the exciton chemical potentials such that

$$\mu_1 = \gamma_{11} n_1 + \gamma_{12} n_2, \ \mu_2 = \gamma_{22} n_2 + \gamma_{12} n_1, \qquad (\text{B3})$$

where γ_{ij}'s are interacting constants. Based on the simulations presented in Figs. 3.4(a) and 3.4(d) of the main text, we set the constants to be $\gamma_{11} = 9.3$, $\gamma_{22} = 11$, and $\gamma_{12} = -0.2$, all in units of 10^{-11} meV cm^{-2}. [Note that the intra-CQW coupling constants are 1/3 of the plate capacitor values, i.e., $\gamma_{kk} = \left(\frac{1}{3}\right)(4\pi e^2 d_k/\epsilon)$.] We developed a computer program that solves these coupled equations on a discrete grid of x as a function of the time-variable t, starting from initial conditions $n_1 = n_2 \equiv 0$. To get a relation between the laser powers and the generation rates, we fitted the shifts $E_k \approx \mu_k$ of the exciton emission energies measured as functions of the laser power to the results of these simulations. We estimated the diffusion coefficients D_k by fitting the calculated width of the IX$_1$ and IX$_2$ exciton clouds to the measured widths of these clouds generated selectively by L$_1$ or L$_2$.

As outlined in the main text, the simulations show that the IX_1 cloud attracts to the IX_2 cloud (Fig. 3.5), in qualitative agreement with the attraction observed in the experiment (Fig. 3.3). In comparison, both our experimental measurements (Fig. 3.8) and our theoretical simulations (Fig. 3.9) show that the two clouds of repulsively interacting IX_2 repel each other.
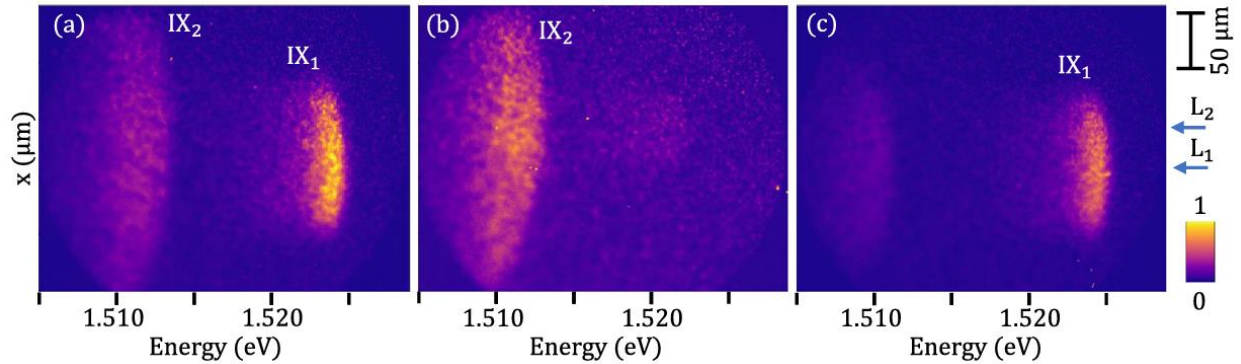

Figure 3.10: Position-energy images of IX luminescence. (a) Both L_2 and L_1 lasers are on. (b) Only L_2 is on. (c) Only L_1 is on. The arrows indicate the excitation spot positions of the L_2 and L_1 lasers resonant to direct excitons in 15-nm CQW and 12-nm CQW, respectively. L_2 generates IX_2. L_1 generates IX_1 and a smaller concentration of IX_2. The laser powers $P_{L1} = 10$ μW, $P_{L2} = 250$ μW. Gate voltage $V_g = -2.0$ V and temperature $T = 1.7$K.

3.5.4 Position-Energy Luminescence Images

The differential x-energy image [Fig. 3.1(b)] is obtained by subtracting the x-energy images created by only L_1 on [Fig. 3.10(c)] and by only L_2 on [Fig. 3.10(b)] from the x-energy image created by both lasers on simultaneously [Fig. 3.10(a)].
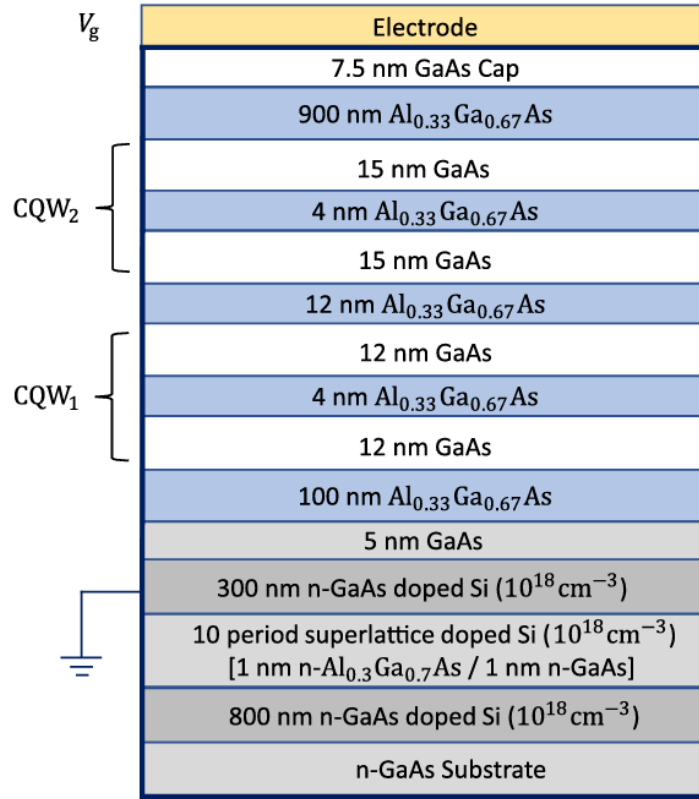
V_g	Electrode
	7.5 nm GaAs Cap
	900 nm $Al_{0.33}Ga_{0.67}As$
CQW$_2$	15 nm GaAs
	4 nm $Al_{0.33}Ga_{0.67}As$
	15 nm GaAs
	12 nm $Al_{0.33}Ga_{0.67}As$
CQW$_1$	12 nm GaAs
	4 nm $Al_{0.33}Ga_{0.67}As$
	12 nm GaAs
	100 nm $Al_{0.33}Ga_{0.67}As$
	5 nm GaAs
	300 nm n-GaAs doped Si ($10^{18} cm^{-3}$)
	10 period superlattice doped Si ($10^{18} cm^{-3}$) [1 nm n-$Al_{0.3}Ga_{0.7}As$ / 1 nm n-GaAs]
	800 nm n-GaAs doped Si ($10^{18} cm^{-3}$)
	n-GaAs Substrate

Figure 3.11: Cross section of the two-CQW heterostructure. The thicknesses and doping concentrations of the layers are indicated.

3.5.5 Cross Section of the Heterostructure

The cross section of the two-CQW heterostructure showing the thicknesses and doping concentrations of the layers is presented in Fig. 3.11.

3.6 Acknowledgements

dissertation author was the first author. The co-authors in these publications directed, supervised,

and co-worked on the research which forms the basis of this chapter.

Chapter 4: Fermi edge singularity in neutral electron-hole system

4.1 Introduction

The theory of an ultracold neutral electron-hole (e-h) system considers two density regimes. At low e-h densities, $n << 1/a_B^D$ (a_B is the exciton Bohr radius, D the dimensionality), electrons and holes bind to hydrogen-like pairs – excitons, which form a Bose-Einstein condensate at low temperatures [19]. In dense electron-hole systems, $n \gtrsim 1/a_B^D$, e-h plasma can be realized and, at low temperatures, the theory predicts Cooper-pair-like excitons at the Fermi energy and a BCS-like exciton condensation [20].

E-h systems can be created by optical excitation. The advantage of the optically created e-h systems is the ability to tune the density and, in turn, the parameter na_B^D within orders of magnitude by the excitation power P_{ex}. In particular, this allows exploring both the BEC and BCS-like exciton condensates and the crossover between them. 2D e-h systems in layered semiconductor heterostructures offer an additional advantage of tailoring the system parameters by the layer design.

For a dense 2D e-h plasma with $n \gtrsim 1/a_B^2$ at temperatures lower than the electron and hole Fermi energies and higher than the condensation temperature, the photoluminescence (PL) spectrum is step-like corresponding to the step-like 2D density of states, and the PL linewidth is approximately the sum of the electron and hole Fermi energies, $\Delta \sim E_{Fe} + E_{Fh}$ [84]. In contrast, in the low-density regime, the exciton PL linewidth is determined by the homogeneous and inhomogeneous broadening and is significantly smaller than the e-h plasma PL linewidth in high-quality heterostructures [18]. The BCS-like condensation in the ultra-cold e-h plasma with Cooper-pair-like excitons at the Fermi energy should be accompanied by a PL intensity enhancement at

the Fermi level of the step-like e-h plasma PL line, similar to the Fermi edge singularity in a Fermi-gas of electrons [85] [86]. The latter phenomenon was observed in PL spectra of a 2D electron gas for a weak optical excitation with the number of photoexcited electrons and holes much smaller than the electron gas density, that is in a system, which can be described as a single optically created hole in a Fermi sea of electrons.

In contrast to the generation of "a single hole" in a dense electron gas [86], the realization of a neutral dense e-h system by optical excitation requires the generation of a high number of electrons and holes that causes the problem of heating. Due to e-h recombination, the temperature of an optically created e-h system (T_{eh}) exceeds the semiconductor lattice temperature and lowering T_{eh} below the condensation temperature, in particular at high e-h densities, is challenging. For instance, for neutral dense plasmas generated in single InGaAs/InP [84]or InGaAs/GaAs [81] [87] quantum wells in experiments at T ~ 2 K, the effective e-h temperature reached and exceeded ~ 100 K, well above both the lattice temperature and the temperature needed for the realization of the Cooper-pair like excitons and BCS-like exciton condensation [20].

The other requirement for the realization of Cooper-pair-like excitons at the Fermi energy and BCS-like exciton condensation is matching of the electron and hole Fermi surfaces [2]. For equal electron and hole densities, the Fermi momenta of electrons and holes are equal (Fig. 4.1a), that is required for matching the Fermi surfaces. This matching of the electron and hole Fermi surfaces in neutral e-h system is different from the Fermi edge singularity for a hole in a Fermi sea of electrons where the suppression of hole kinetic energy, a flat hole band or hole localization, is required [85] [86].
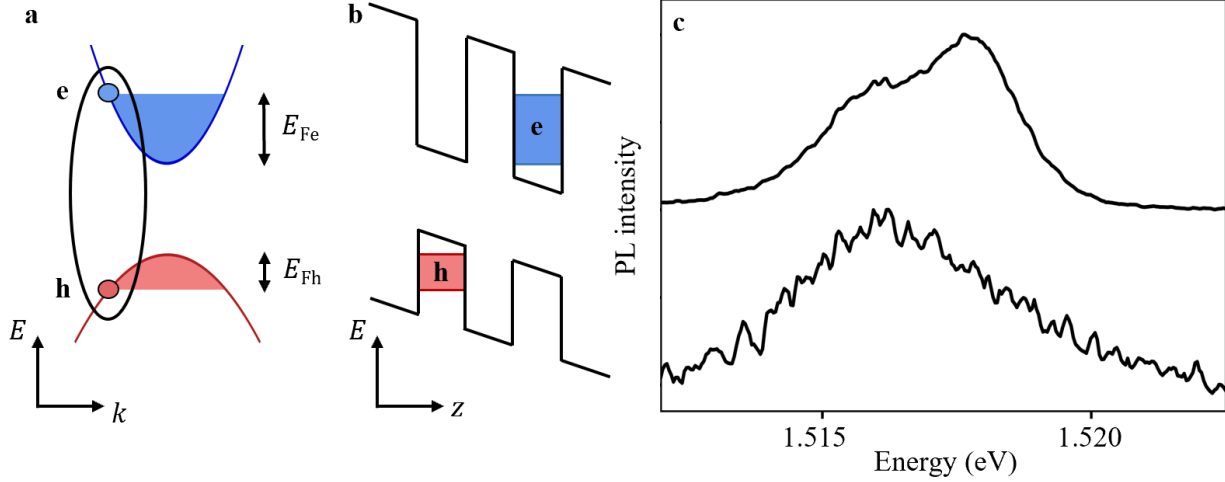
Figure 4.1: (a) Diagram showing Cooper-pair-like excitons (oval) with electrons (e) and holes (h) at the Fermi energy in neutral dense e-h system. (b) Diagram of the CQW heterostructure. Electrons and holes in I-EHP are confined in separated layers. (c) I-EHP PL spectra at $T = 2$ K (top) and 20 K (bottom). The laser excitation power $P_{ex} = 24$ mW. The Fermi edge singularity is observed in cold I-EHP.

4.2 Experimental Methods

To create cold e-h systems, we work with heterostructures with separated electron and hole layers (Fig. 4.1b). In these heterostructures, spatially indirect excitons (IXs), also known as interlayer excitons, are formed by electrons and holes confined in separated layers [34]. The layer separation increases the e-h recombination time that allows cooling the optically generated e-h system to low temperatures [88]. The other advantage of the separated electron and hole layers is the overall enhancement of energy per e-h pair with density that is outlined below. This enhancement stabilizes the exciton state against the formation of e-h droplets [35] [36] [37] [89], which otherwise may form the ground state [90]. Earlier studies of cold IXs concerned the low-density regime where IXs are hydrogen-like pairs. An overview of experimental studies of IX condensation in the low-density regime and phenomena in the IX condensate can be found in Ref. [24].
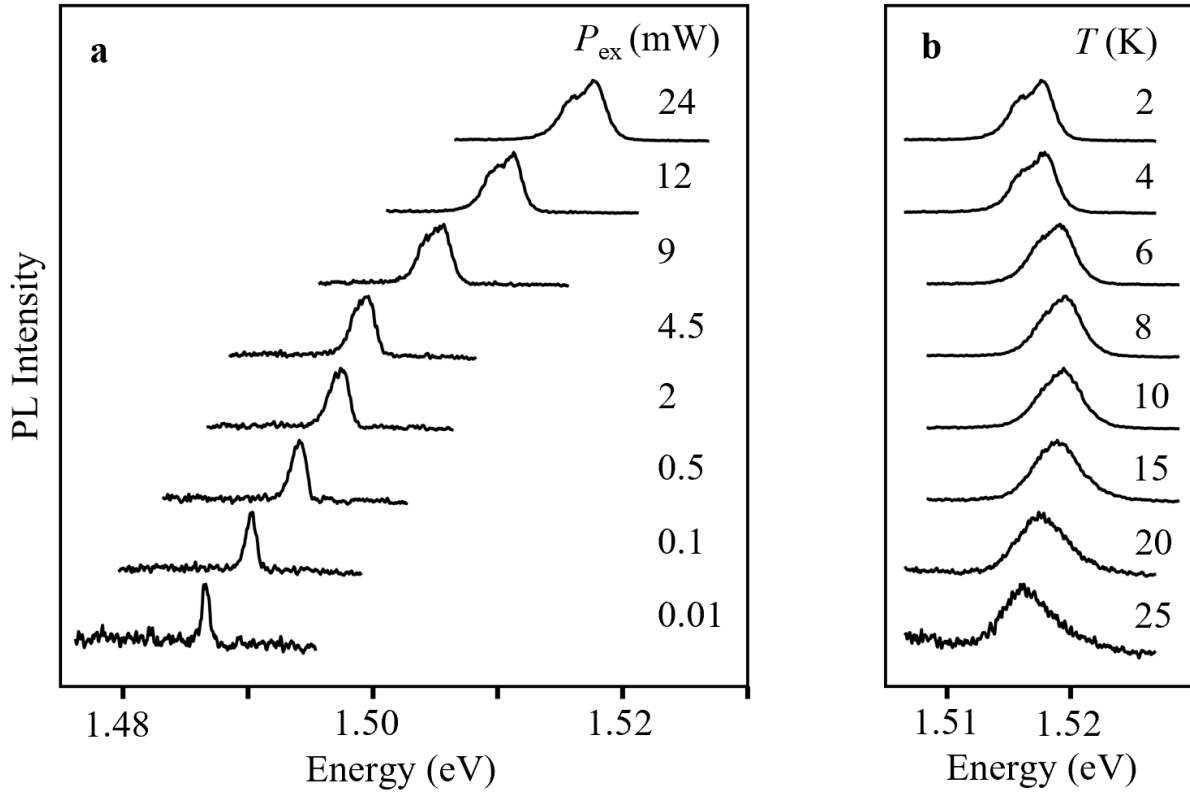
Figure 4.2: Density and temperature dependence of PL spectra. (a) PL spectra vs. the laser excitation power P_{ex}. T = 2 K. The e-h densities estimated from the energy shift n ~ 11, 9, 7, 5, 4, 3, 1, 0.3 × 10^{10} cm^{-2} (from top to bottom). The spectra show the crossover from hydrogen-like IXs at low densities to I-EHP with the Fermi edge singularity at high densities. (b) PL spectra vs. temperature. P_{ex} = 24 mW. The Fermi edge singularity vanishes at high temperatures.

In this work, we study ultracold neutral spatially indirect e-h plasma (I-EHP) in separated electron and hole layers in a GaAs/AlGaAs coupled quantum well (CQW) heterostructure. The electrons and holes are confined in 15 nm GaAs QWs separated by 4 nm AlGaAs barrier. The long e-h recombination lifetimes [τ ~ μs, Fig. 4.5a] due to the separation between the electron and hole layers allow for cooling the plasma to low temperatures. The creation of cold IEHP is facilitated by separating the e-h plasma from the laser excitation in space and time: (i) The measurements are performed δt = 300 ns after the laser excitation pulse within τ_w = 50 ns window (Fig. 4.5a). This delay δt is sufficient for cooling the photoexcited e-h system to low temperatures close to the lattice

40

temperature [88]. At the same time, $\delta t \sim \tau$ and $\tau_w << \tau$ enable the density staying high and nearly constant during the measurements. (ii) The measurements are performed $\sim$ 50 μm away from the edge of the mesa-shaped laser excitation spot (Fig. 4.5b). This separation further facilitates cooling of the photoexcited e-h system. At the same time, the density in the signal detection region does not drop substantially in comparison to the excitation region since the separation is shorter than the I-EHP (and IX) propagation length in the heterostructure (Fig. 4.5b). To further reduce the heating of e-h system, the laser excitation is resonant to the direct exciton energy ($E_{ex} \sim 1.545$ eV). The resonant excitation increases absorption for a fixed P_{ex} and minimizes the energy of photoexcited e-h pairs [77]. The laser pulses are 800 ns on, 400 ns off. The off time is longer than δt to enable the cooling, yet is as short as possible, just longer than $\delta t + \tau_w$, to enhance the density for a given P_{ex}.

In the experiments, the densities of photoexcited eh system are controlled by P_{ex} from the low-density IX regime to the high density I-EHP regime. In the high density regime, we observed a broad I-EHP line with a linewidth exceeding the IX binding energy [37] [91] and increasing with density (Figs. 4.1 and 4.2a). The simulation of the I-EHP PL line without taking into account the Fermi edge singularity due to the Cooper-pair-like excitons at the Fermi energy are presented in Fig. 4.8 in section 4.4.3. These simulations show step-like spectra with the linewidth $\Delta \sim E_{Fe} + E_{Fh}$, similar to the spectra of spatially direct EHP in single QWs in earlier studies [84].

4.3 Results

At high temperatures, the I-EHP PL line (Fig. 4.1c bottom) is typical for plasmas above the condensation temperature [84] and the line shape is consistent with the simulations with no Fermi edge singularity (Fig. 4.8). At low temperatures, we observed a strong enhancement of the

PL intensity at the Fermi energy of cold plasma (Fig. 4.1c top) that evidences the emergence of excitonic Fermi edge singularity. The temperature and density dependence of the spectra are consistent with the many-body origin of this enhancement.

At the lowest densities, the IX linewidth ~ 0.6 meV (Fig. 4.2a). The small IX linewidth indicates a low disorder in the heterostructure. With increasing e-h density, we observe a transition from the ultracold gas of hydrogen like IXs, with the narrow PL line at low e-h densities to the ultracold I-EHP with the Fermi edge singularity due to the Cooper-pair-like excitons at the Fermi energy at high e-h densities (Fig. 4.2a). The transition is smooth, consistent with the theory predicting a crossover from hydrogen-like excitons to Cooper-pair-like excitons with increasing density [92].
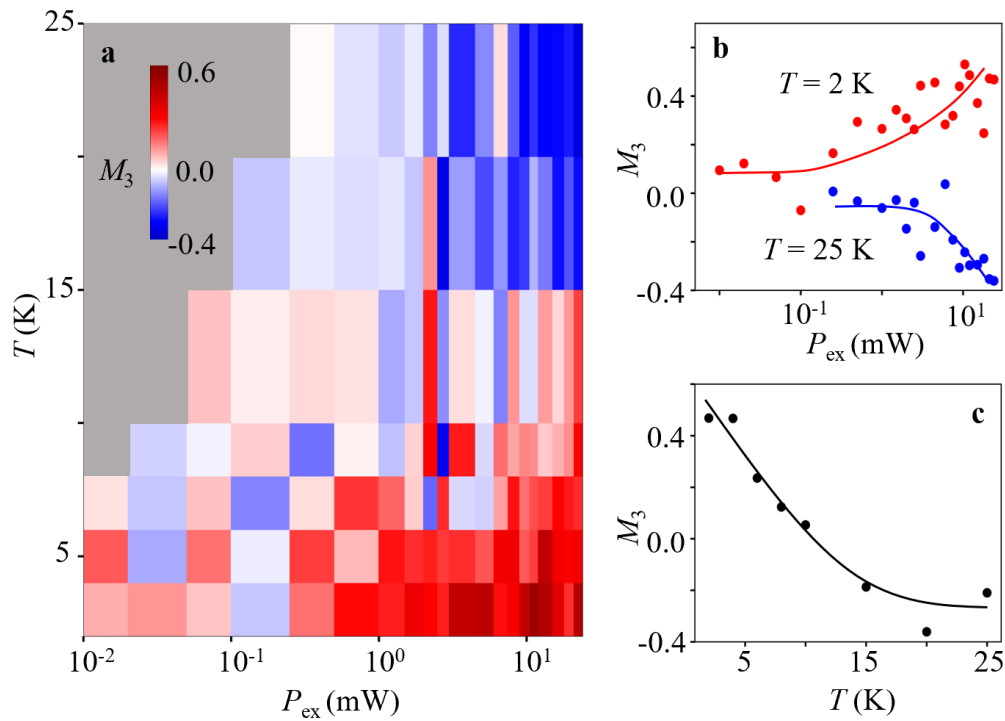

Figure 4.2: The spectrum skewness M3. (a) M3 vs. the laser excitation power P_{ex} and temperature. (b) M_3 vs. P_{ex} at T = 2 K and 25 K. (c) M_3 vs. temperature at $P_{ex} = 24$ mW. The lines are guides to the eye. The Fermi edge singularity characterized by high positive M_3 is observed in dense I-EHP at low temperatures.

The overall shift of the PL energy (Fig. 4.2a) is caused by the separation between the electron and hole layers and can be approximated by the "capacitor" formula $\delta E = 4\pi e^2 dn/\varepsilon$, where d is the separation between the layers, ε the dielectric constant [35]. This approximation becomes increasingly more accurate with increasing density [8]. The e-h density n estimated from the energy shift δE is close to n estimated from the plasma PL linewidth $\Delta \sim E_{Fe} + E_{Fh} = \pi\hbar^2 n(1/m_e + 1/m_h)$, where m_e and m_h are the electron and hole effective masses (Fig. 4.7 in section 4.4.3).
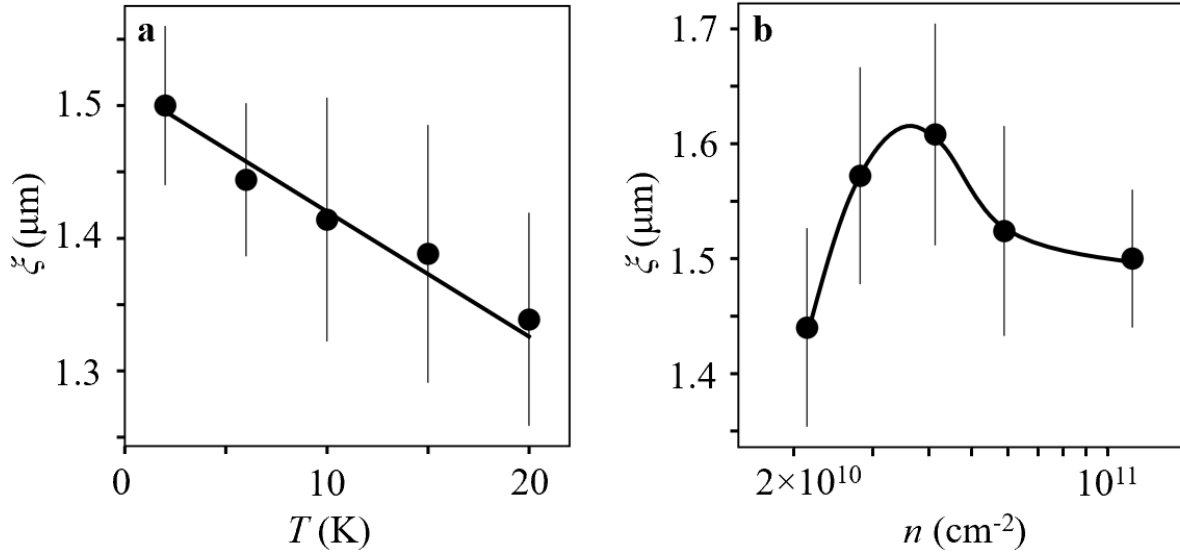

Figure 4.4: Density and temperature dependence of the coherence length. (a) ξ vs. temperature. The density n estimated from the energy shift $n \sim 10^{11}$ cm^{-2}. $P_{ex} = 24$ mW. (b) ξ vs. n. $P_{ex} = 0.2$, 0.5, 2.5, 7.5, 24 mW (from left to right). T = 2 K. The lines are guides to the eye.

The Fermi edge singularity vanishes with increasing temperature (Fig. 4.2b). This is quantified in Fig. 4.3 by the spectrum skewness M_3. A higher intensity at the high-energy (low-energy) side of the PL line, such as in the top (bottom) spectrum in Fig. 4.1c, corresponds to positive (negative) M$_3$. Figure 4.3 shows that the Fermi edge singularity characterized by high positive M$_3$ is observed in the dense I-EHP at low temperatures, that is in the high-P_{ex} – low-T

part of the $P_{ex} - T$ diagram. A similar n − T diagram with the density n estimated from the shift δE is shown in Fig. 4.9 in 4.4.3.

We also measured the coherence length by shift-interferometry. Similar measurements for IXs in the low-density regime detected IX spontaneous coherence and, in turn, the IX BEC in earlier studies [3]. In the shift-interferometry measurements, the emission images produced by each of the two arms of Mach-Zehnder interferometer are shifted with respect to each other to probe the interference between the emission of I-EHP (or IXs) spatially separated by δx in the layer plane. The amplitude of interference fringes gives the first order coherence function $g_1(\delta x)$ and the width of $g_1(\delta x)$, the coherence length, quantifies spontaneous coherence in the system [3] [93].

The coherence vanishes with increasing temperature (Fig. 4.4a). With increasing P_{ex} and, in turn, the density, the coherence length first increases, reaches maximum, and then reduces (Fig. 4.4b). The density dependence is qualitatively consistent with the theory predicting that coherence increases with density in the BEC regime, reaches maximum at the BEC–BCS crossover, and reduces with density in the BCS regime [92].

According to the theory, the BEC–BCS crossover should occur at the densities close to the density of the Mott transition $n_M \sim 0.2/a_B{}^2$ [55] [57] [61] [94]. The density $n \sim 4 \times 10^{10}$ cm^{-2} where the maximum coherence is observed (Fig. 4.4b) is qualitatively consistent with this theoretical estimate. For instance, for $a_B \sim 20$ nm estimated for IXs in Ref. [95], $n_M \sim 0.2/a_B{}^2 \sim 5 \times 10^{10}$ cm^{-2}. In the density range corresponding to the onset of the BCS regime n $\gtrsim 4 \times 10^{10}$ cm^{-2} ($P_{ex} \gtrsim 2$ mW), the PL lineshape start revealing the intensity enhancement at the high-energy side, indicating the Fermi edge singularity (Fig. 4.2a).

The coherence length (Fig. 4.4) reaches significantly higher values than in a classical gas [$\xi_{classical} \sim \lambda_{dB} \sim 0.1$ μm at T = 2 K for IXs in GaAs CQW, $\lambda_{dB} = (2\pi\hbar^2/mT)^{1/2}$ is the thermal de Broglie wavelength]. The maximum ξ (Fig. 4.4) is smaller than in the measurements of IXs in the low-density regime in the heterostructure with smaller d, where ξ reaches several microns [3]. A higher ξ in that work may be related, in particular, to a weaker dipolar interaction and a specific electro-optical IX generation with holes optically generated and electrons electronically injected in localized areas [3].

A relation of the studied system to other systems is outlined below. The Fermi edge singularity in neutral e-h system due to Cooper-pair-like excitons at the Fermi energy and BCS-like exciton condensation are related to excitonic insulators [20] [96] [97] [98]. In contrast to optically created e-h systems in semiconductors, such as the system considered in this work, the excitonic insulators generally form in semimetals or in narrow-gap semiconductors with no optical generation. The nature of BCS-like exciton condensates in optically created e-h systems and excitonic insulators in semimetals is similar. Excitonic insulators are actively studied [99] [100] [101] [102] [103] [104] [105] [106] [107] [108] [109] [110] [111] [112] [113] [114].

The other system, which allows studying the BEC– BCS crossover, is a system of ultracold atoms with controlled interactions [115]. In comparison, in the ultracold e-h system studied here, the density and, in turn, the parameter na_B^2 is controlled. The density increase allows to go from the low-density regime of hydrogen-like excitons to the high-density regime of Cooper-pair-like excitons and the regimes are revealed by the distinct PL line shapes with the high-density regime characterized by the Fermi edge singularity due to the Cooper-pair-like excitons at the Fermi energy.

In summary, we found a strong enhancement of photoluminescence intensity at the Fermi energy of the neutral dense ultracold e-h system that evidences the emergence of excitonic Fermi edge singularity due to the Cooper pair-like excitons at the Fermi energy.

4.4 Supplemental Information

4.4.1 CQW Heterostructure

The CQW heterostructure (Fig. 4.1b) is grown by molecular beam epitaxy. CQW consists of two 15-nm GaAs QWs separated by a 4-nm $Al_{0.33}Ga_{0.67}As$ barrier. n+ GaAs layer with $n_{Si} \sim 10^{18}$ cm^{-3} serves as a bottom electrode. The CQW is positioned 100 nm above the n+ GaAs layer within the undoped 1-µm-thick $Al_{0.33}Ga_{0.67}As$ layer. The CQW is positioned closer to the homogeneous bottom electrode to suppress the fringing in-plane electric field in excitonic devices [76]. The top semitransparent electrode is fabricated by applying 2-nm Ti and 7-nm Pt on a 7.5-nm GaAs cap layer. Applied gate voltage $V_g = -2.5$ V creates an electric field in the z direction.
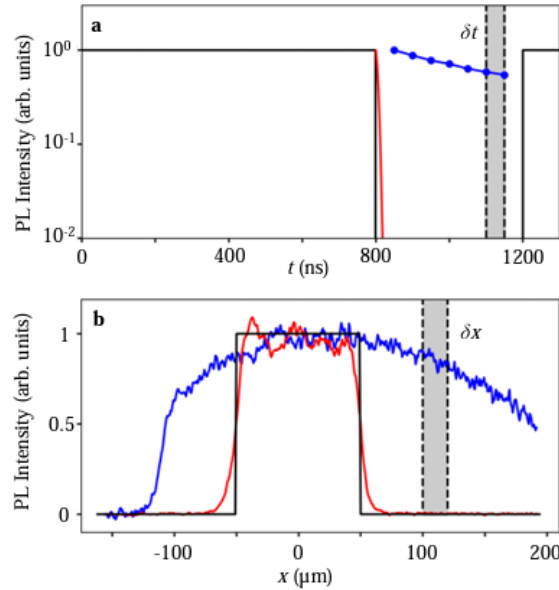
Figure 4.5: Optical measurements. (a) The e-h system is generated by laser pulses 800 ns on, 400 ns off (shown schematically by blue line). The measurements are performed $\delta t = 300$ ns after the laser excitation pulse within $\tau_\mathrm{w} = 50$ ns window (gray area). (b) The laser excitation spot is mesa-shaped (shown schematically by blue line). The measurements are performed ~ 50 µm away from the edge of the mesa-shaped laser excitation spot within ~ 20 µm window (gray area). $x \sim -100$ µm corresponds to the device edge. The DX PL (red line) closely follows the laser excitation in time (a) and space (b) due to the short DX lifetime. The I-EHP PL (black line and dots) extends in time (a) and space (b) due to the long I-EHP lifetime.
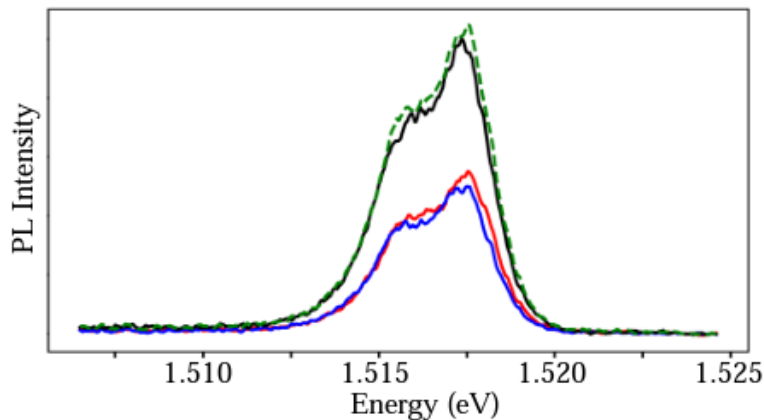
Figure 4.6: Variation of the spectra within the signal accumulation window. The I-EHP spectrum measured during the 50 ns window (black line) and during the first half (red line) and within the second half (blue line) of the window. The sum of the spectra within the half-windows (green dashed line) is close to the spectrum within the window (black line). These measurements show that the spectrum variation during the window is negligibly small.

47

4.4.2 Optical Measurements

The experiments are designed to facilitate lowering the temperature of the optically generated e-h system, as outlined in the main text. The e-h system is generated by a Ti:Sapphire laser resonant to the direct exciton (DX) energy ($E_{ex} \sim 1.545$ eV). An AOM is used for making laser pulses 800 ns on, 400 ns off (Fig. 4.5a). The measurements are performed $\delta t = 300$ ns after the laser excitation pulse within $\tau_w = 50$ ns window (Fig. 4.6a). The mesa-shaped laser excitation spot with ~ 100 μm diameter is formed using an axicon. The measurements are performed ~ 50 μm away from the edge of the mesa-shaped laser excitation spot within ~ 20 μm window (Fig. 4.6b). The DX PL closely follows the laser excitation in time (Fig. 4.6a) and space (Fig. 4.61b) due to the short DX lifetime. The I-EHP (and IX) PL extends in time (Fig. 4.6a) and space (Fig. 4.6b) due to the long I-EHP (and IX) lifetime.

The 50 ns window is long enough to collect sufficient I-EHP (or IX) signal yet much shorter than the I-EHP (or IX) lifetime so the signal variation during the window is negligibly small. To verify this, the measurements were performed within the first half and within the second half of the window and these measurements show similar spectra (Fig. 4.6).

The PL spectra are measured using a spectrometer with resolution 0.2 meV and a liquid-nitrogen-cooled CCD coupled to a PicoStar HR TauTec time-gated intensifier. The experiments are performed in a variable temperature 4He cryostat.
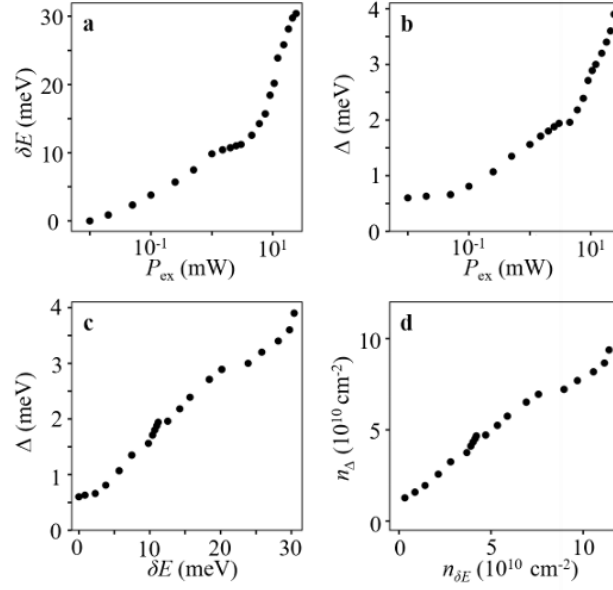
Figure 4.7: PL energy shift and linewidth. (a) The PL energy shift δE vs. P_{ex}. δE is counted from the IX energy at the lowest P_{ex}. (b) The PL linewidth Δ(full-width-half-maximum) vs. P_{ex}. (c) Δ vs. δE. (d) n estimated from Δ vs. n estimated from δE. T = 2K for all data. The estimates use $\delta E = 4\pi e^2 dn/\varepsilon$ and $\Delta \sim E_{Fe} + E_{Fh} = \pi\hbar_2 n(1/m_e + 1/m_h)$. The estimates from δE and from Δ give similar n.
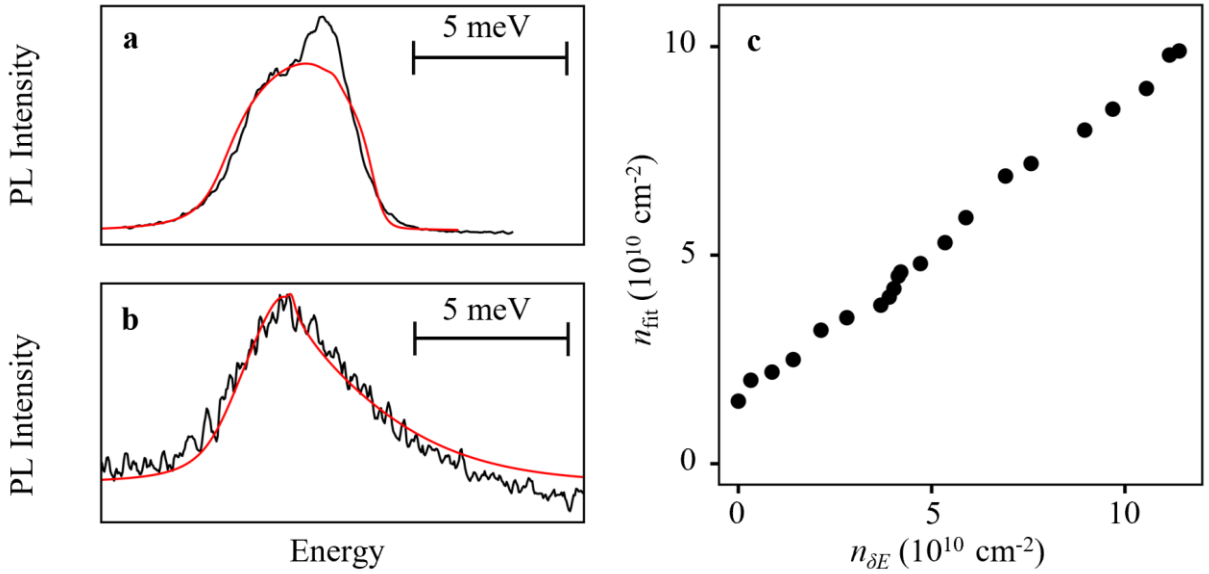
Figure 4.8: Simulations of I-EHP PL spectra. (a,b) The simulated I-EHP PL spectra without taking into account the Fermi edge singularity (redlines) and the measured I-EHP PL spectra (blacklines). T=2K and P_{ex}=24mW, T_{fit} = 2K and n_{fit} =10^{11} cm^{-2} (a). T = 25K and P_{ex} = 24mW, T_{fit} = 25K and n_{fit} = 7.6×10^{10}cm^{-2} (b). (c) n estimated from the PL spectrum fit vs. n estimated from δE, T = 2K.

4.4.3 PL Energy Shift and Line shape

The density n in I-EHP can be estimated from the PL energy shift δE using the "capacitor" formula $\delta E = 4\pi e^2 dn/\varepsilon$. n in I-EHP can be also estimated from the PL linewidth $\Delta \sim E_{Fe} + E_{Fh} = \pi\hbar^2 n(1/m_e + 1/m_h)$. The estimates from δE and from Δ give similar n in the high density regime, $n \gtrsim 4\times10^{10}$ cm^{-2} (Fig. 4.7d). The estimates extended to the low-density regime show a deviation from this similarity, increasing for lower densities (Fig. 4.7d). The deviation is expected since in the low density regime, the equation for δE is less accurate and Δ is determined by the homogeneous and inhomogeneous IX broadening, as outlined previously.

The I-EHP PL spectra are simulated without taking into account the Fermi edge singularity and compared with the measured I-EHP PL spectra (Fig. 4.8). The simulations are outlined below. Due to the small photon momentum, the optical transition occur for the same absolute values of electron and hole momenta $k_e=k_h$. For the constant 2D density of states, the PL intensity at energy $E_i = \frac{\hbar^2 k_i^2}{2m_e} + \frac{\hbar^2 k_i^2}{2m_h}$ is determined by the product of the electron and hole distribution functions $I(E_i) \propto f_e(k_i)f_h(k_i)$, where E_i is counted from the lowest PL energy, $k_i=k_e=k_h$, $f_{e,h}=(\exp\frac{\hbar^2\left(k_i^2-k_f^2\right)}{2m_{e,h}k_B T} + 1)^{-1}$, k_F the Fermi momentum. For low temperatures $k_B T \ll E_{Fe}$, E_{Fh}, the PL line $I(E_i)$ is step-like with the sharp steps both on the low-energy side and the high-energy side and the width $\Delta \sim E_{Fe} + E_{Fh} = E_F$. The step sharpness on the high-energy side is determined by the temperature. To account for the finite step sharpness on the low-energy side the following approximation is used. $I(E_i)$ is convolved with $\frac{\gamma(E_i)}{\pi}\frac{1}{(E-E_i)^2-\gamma(E_i)^2}$ describing the damping of one-particle states [116], where the broadening parameter $\gamma(E_i)$ is assumed to decrease to zero at the Fermi level as $(E_F-E_i)^2$ [117].

At high temperatures, the simulated and measured I-EHP spectra are close, with the intensity reduction at the high-energy side following the thermal distribution (Fig. 4.8b). At low temperatures, the simulations show step-like I-EHP spectra with the linewidth $\Delta \sim E_{Fe} + E_{Fh}$, similar to the spectra of spatially direct EHP in single QWs [84], and the measured I-EHP PL is strongly enhanced at the Fermi energy in comparison to the simulations due to the Fermi edge singularity (Fig. 4.8a). For the dense I-EHP, the density n fit estimated from the PL spectrum fit is close to the density estimated from the energy shift δE (Fig. 4.4c). n fit (Fig. 4.4c) is close to the density estimated from the PL linewidth Δ (Fig. 4.3d).

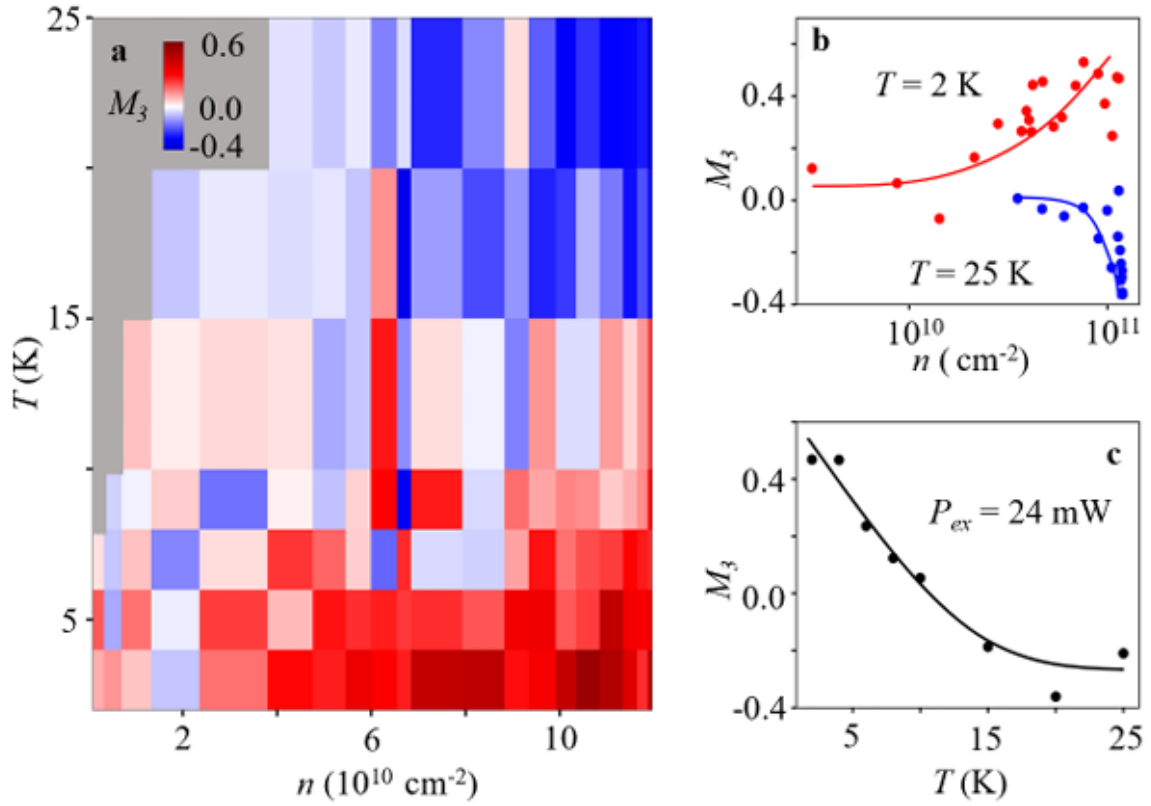**Figure 4.9:** The spectrum skewness M_3. (a) M_3 vs. density and temperature. The density n is estimated from the energy shift $\delta E = 4\pi e^2 dn/\varepsilon$. (b) M_3 vs. n at $T = 2$ K and 25 K. (c) M_3 vs. temperature at $n = 10^{11}$ cm^{-2}. The lines are guides to the eye. The Fermi edge singularity characterized by high positive M_3 is observed in dense I-EHP at low temperatures.

51

4.4.4 The spectrum Skewness M_3

Figure 4.9 shows the spectrum skewness M_3 vs. temperature and density. This figure is similar to Fig. 4.3 showing M_3 vs. temperature and P_{ex}. The density n is estimated from the energy shift $\delta E = 4\pi e^2 dn/\varepsilon$. Figure 4.9 shows that the Fermi edge singularity characterized by high positive M_3 is observed in the dense I-EHP at low temperatures, that is in the high-n – low-T part of the $n - T$ diagram.

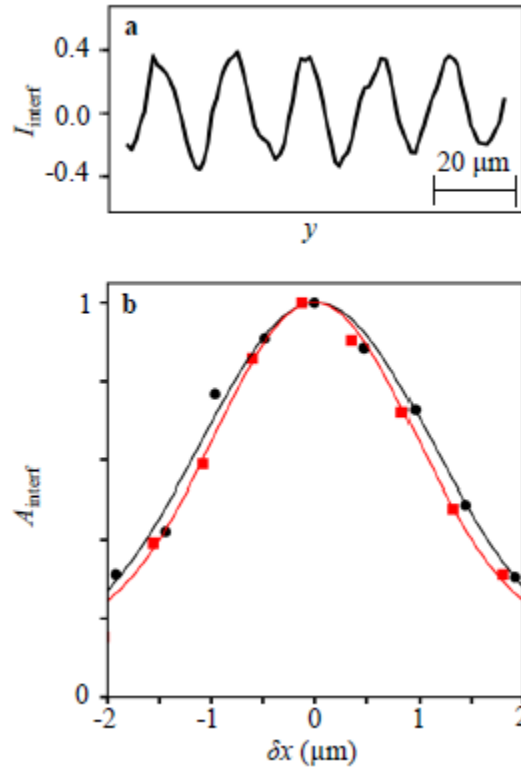**Figure 4.10:** Shift-interferometry measurements. (a) Interference fringes $I_{interf}(y)$ for $\delta x = 1.5$ μm, $T = 2$ K, $P_{ex} = 2.5$ mW. (b) The amplitude of interference fringes A_{interf} vs. δx for $P_{ex} = 2.5$ mW (black points) and 0.2 mW (red squares), $T = 2$ K. Gaussian fits are shown by the black and red lines, respectively.

4.4.6 Shift-Interferometry measurements

In the shift-interferometry measurements, a Mach- Zehnder interferometer is added in the signal detection path as in Ref. [3]. The spectrometer grating is replaced by a mirror and an interference filter of linewidth 5 nm adjusted to the I-EHP (or IX) PL wavelength is added to select the entire I-EHP (or IX) PL line for the studied P_{ex} and T. The rest of the laser excitation and signal detection, outlined above, is kept unchanged.

The emission images produced by each of the two arms of the Mach-Zehnder interferometer are shifted relative to each other along x to measure the interference between the emission of I-EHPs (or IXs), which are separated by δx in the layer plane. $I_{\text{interf}} = (I_{12} - I_1 - I_2)/(2\sqrt{I_1 I_2})$ is calculated from the measured PL intensity I_1 for arm 1 open, I_2 for arm 2 open, and I_{12} for both arms open (Fig. 4.10a). In "the ideal experiment", the amplitude of interference fringes $A_{\text{interf}}(\delta x)$ gives the first order coherence function $g_1(\delta x)$ and the width of $g_1(\delta x)$, the coherence length, quantifies spontaneous coherence in the system [3]. In practice, the measured $A_{\text{interf}}(\delta x)$ is given by the convolution of $g_1(\delta x)$ with the point-spread function (PSF) of the optical system in the experiment [93]. The CQW contain no point source for the precise measurement of PSF. NA = 0.27 of the objective in the experiment gives a lower estimate for PSF width $\xi_{\text{PSF}} \sim 0.9$ μm for the optical system. The dependence of ξ on the parameters shows that the coherence length in the e-h system is sufficiently large in comparison to the spatial resolution of the optical system ξ_{PSF}. Otherwise, the measured ξ would be determined by ξ_{PSF} and practically would not depend on the parameters [93]. Figure 4.10b shows examples of the measured $A_{\text{interf}}(\delta x)$. ξ are taken as the half-widths at $1/e$ height of Gaussian fits to $A_{\text{interf}}(\delta x)$.

4.5 Acknowledgements

Bibliography

[1] J. Frenkel. On the Transformation of light into Heat in Solids. I, *Phys. Rev.* **37**, 17 (1931).

[2] J. Frenkel. On the Transformation of Light into Heat in Solids. II, *Phys. Rev.* **37**, 1276, (1931).

[3] A. A. High, J. R. Leonard, A. T. Hammack, M. M. Fogler, L. V. Butov, A. V. Kavokin, K. L. Campman, and A. C. Gossard. Spontaneous coherence in a cold exciton gas, *Nature* **483**, 584 (2012).

[4] L. V. Butov. Excitonic Devices, *Superlattices Microstructures* **108**, 2 (2017).

[5] L. V. Butov, A. A. Shashkin, V. T. Dolgopolov, K. L. Campman and A. C. Gossard. Magneto-optics of the spatially separated electron and hole layers in GaAs/Al$_x$Ga$_{1-x}$As coupled quantum wells. *Phys. Rev. B* **60**, 8753 (1999).

[6] L. V. Butov. Condensation and pattern formation in cold exciton gases in coupled quantum wells. *J. Phys: Condensed Matter* **16**, R1577R1613 (2004).

[7] A. Alexandrou, J. A. Kash, E. E. Mendez, M. Zachau, J. M. Hong, T. Fukuzawa, Y. Hase. Electric-field effects on exciton lifetimes in symmetric coupled GaAs/Al0:3Ga0:7As double quantum wells. *Phys. Rev. B* **42**, 9225 (1990).

[8] D. J. Choksy, Chao Xu, M. M. Fogler, L. V. Butov, J. Norman, and A. C. Gossard. Attractive and repulsive dipolar interaction in bilayers of indirect excitons. *Phys Rev B* **103**, 045126 (2021).

[9] C. J. Dorow, M. W. Hasling, D. J. Choksy, J. R. Leonard, L. V. Butov, K. W. West, L. N. Pfeiffer. High-mobility indirect excitons in wide single quantum well. *App. Phys Lett* **113**, 212102 (2018).

[10] M. Remeika, J. C. Graves, A. T. Hammack, A. D. Meyertholen, M. M. Fogler, and L. V. Butov, M. Hanson and A. C. Gossard. Localization-Delocalization Transition of Indirect Excitons in Lateral Electrostatic Lattices. *Phys. Rev. Lett.* **102**, 186803 (2009).

[11] M. Hagn, A. Zrenner, G. Böhm, and G. Weimann. Electric-field-induced exciton transport in coupled quantum well structures. *App. Phys. Lett.* **67**, 232 - 234 (1995).

[12] L.V. Butov and A.I. Filin. Anomalous transport and luminescence of indirect excitons in AlAs/GaAs coupled quantum wells as evidence for exciton condensation. *Phys Rev B* **58**, 1980, (1998).

[13] A.V. Larionov, V.B. Timofeev, J. Hvam, and K. Soerensen. Interwell excitons in GaAs/AlGaAs double quantum wells and their collective properties. *J. Exp. Theor. Phys.* **90**, 1093 (2000).

[14] L.V. Butov, A. Zrenner, G. Abstreiter, G. Böhm, G. Weimann. Condensation of indirect excitons in coupled AlAs/GaAs quantum wells, *Phys. Rev. Lett.* **73**, 304 (1994).

[15] S. G. Tikhodeev. On the Bose-Einstein condensation of particles with finite lifetime - as demonstrated by excitons. *Solid State Communications* **72**, 1075 (1989).

[16] A. L. Ivanov, C. Ell, and H. Haug. Phonon-assisted Boltzmann kinetics of a Bose gas: Generic solution for $T < T_c$. *Phys. Rev. E* **55**, 6363 (1997).

[17] A. L. Ivanov, P. B. Littlewood, and H. Haug. Bose-Einstein statistics in thermalization and photoluminescence of quantum-well excitons. *Phys. Rev. B* **59**, 5032 (1999).

[18] A. A. High, A. T. Hammack, L. V. Butov, L. Mouchliadis, A. L. Ivanov, M. Hanson, and A. C. Gossard. Indirect excitons in elevated traps. *Nano Letters* **9**, 2094 (2009).

[19] L.V. Keldysh, A. N. Kozlov. Collective properties of excitons in semiconductors. *Soviet Physics JETP* **27**, 521 (1968).

[20] L.V. Keldysh, Yu.V. Kopaev. Possible instability of the semimetallic state toward Coulomb interaction. *Soviet Physics, Soldi State* **6**, 2219 (1965).

[21] L. V. Butov, A. C. Gossard, and D. S. Chemla. Macroscopically ordered state in an exciton system. *Nature* **418**, 751 - 754 (2002).

[22] Sen Yang, L.V. Butov, B.D. Simons, K. L. Campman, A.C. Gossard. Fluctuation and commensurability effect of exciton density wave. *Phys. Rev. B* **91**, 245302 (2015).

[23] J.R. Leonard, A.A. High, A.T. Hammack, M.M. Fogler, L.V. Butov, K.L. Campman, A.C. Gossard. Pancharatnam-Berry phase in condensate of indirect excitons. *Nat. Commun.* **9**, 2158 (2018).

[24] J.R. Leonard, Lunhui Hu, A.A. High, A.T. Hammack, Congjun Wu, L.V. Butov, K.L. Campman, A.C. Gossard. Moiré pattern of interference dislocations in condensate of indirect excitons, *Nat. Commun.* **12**, 1175 (2021).

[25] A.A. High, A.T. Hammack, J.R. Leonard, Sen Yang, L.V. Butov, T. Ostatnicky, M. Vladimirova, A.V. Kavokin, T.C.H. Liew, K.L. Campman, A.C. Gossard. Spin currents in a coherent exciton gas. *Phys. Rev. Lett.* **110**, 246403 (2013).

[26] P. Andreakou, S.V. Poltavtsev, J.R. Leonard, E.V. Calman, M. Remeika, Y.Y. Kuznetsova, L.V. Butov, J. Wilkes, M. Hanson, A.C. Gossard. Optically controlled excitonic transistor. *Phys. Lett.* **104**, 091101 (2014).

[27] Y. Y. Kuznetsova, M. Remeika, A. A. High, A. T. Hammack, L. V. Butov, M. Hanson, and A. C. Gossard. All-optical excitonic transistor. *Optics Lett.* **35**, 1587 (2010).

[28] G. Grosso, J. Graves, A. T. Hammack, A. A. High, L. V. Butov, M. Hanson and A. C. Gossard. Excitonic switches operating at around 100 K, *Nat. Phot.* **3**, 577 (2009).

[29] A.A. High, A.T. Hammack, L.V. Butov, and A.C. Gossard, Exciton optoelectronic transistor. *Optics Lett.* **32**, 2466 (2007).

[30] A.A. High, E.E. Novitskaya, L.V. Butov, and A.C. Gossard. Control of Exciton Fluxes in an Excitonic Integrated Circuit, *Science* **321**, 229 (2008).

[31] T. Deilmann, K. S. Thygesen. Interlayer Trions in the $MoSe_2$/WSe_2 van der Waals Heterostructure. *Nano Letters* **18**, 1460 (2018).

[32] D. A. B. Miller, D. S. Chemla, T. C. Damen, A. C. Gossard, W. Wiegmann, T. H. Wood, and C. A. Burrus. Electric field dependence of optical absorption near the band gap of quantum-well structures. *Phys. Rev. B* **32**, 1043 (1985).

[33] H. -J. Polland, L. Schultheis, J. Kuhl, E. O. Göbel, and C. W. Tu. Lifetime Enhancement of Two-Dimensional Excitons by the Quantum-Confined Stark Effect. *Phys. Rev. Lett.* **55**, 2610 (1985).

[34] Lozovik, Y E, and Yudson, V I. A new mechanism for superconductivity: pairing between spatially separated electrons and holes. *Sov. Phys. JETP* **44**, 389 (1976).

[35] D. Yoshioka, and A. H. Macdonald. Double quantum well electron-hole systems in strong magnetic fields. *Phys. Soc. Jpn.* **59**, 4211 (1990).

[36] X. Zhu, P. B. Littlewood, M. S. Hybertsen, and T. M. Rice. Exciton Condensate in Semiconductor Quantum Well Structures. *Phys. Rev. Lett.* **74**, 1633 (1995).

[37] Y. E. Lozovik and O. L. Berman. Phase transitions in a system of spatially separated electrons and holes. *J. Exp. Theor. Phys.* **84**, 1027 (1997).

[38] A. L. Ivanov. Quantum diffusion of dipole-oriented indirect excitons in coupled quantum wells. *Europhysics Lett.* **59**, 586 (2002).

[39] A. L. Ivanov, L. E. Smallwood, A. T. Hammack, S. Yang, L. V. Butov, and A. C. Gossard. Origin of the inner ring in photoluminescence patterns of quantum well excitons. *Europhysics Lett.* **73**, 920 (2006).

[40] Z. Vörös, R. Balili, D.W. Snoke, L. Pfeiffer, and K. West. Long-Distance Diffusion of Excitons in Double Quantum Well Structures. *Phys. Rev. Letters* **94**, 226401 (2005).

[41] A. Gärtner; A. W. Holleitner; J. P. Kotthaus, D. Schuh. Drift mobility of long-living excitons in coupled GaAs quantum Wells. *App. Phys. Lett* **89**, 052108 (2006).

[42] S. Lazić, P.V. Santos, R. Hey. Exciton transport by moving strain dots in GaAs quantum wells. *Physica E* **42**, 2640 (2010).

[43] Gorbunov, A. V., Timofeev, V. B. & Demin, D. A. Electro-optical trap for dipolar excitons in a GaAs/AlAs Schottky diode with a single quantum well. *JETP Lett* **94**, 800 (2011).

[44] M. Alloing, A. Lemaître, E. Galopin, and F. Dubin. Nonlinear dynamics and inner-ring photoluminescence pattern of indirect excitons. *Phys. Rev. B* **85**, 245106 (2012).

[45] S. Lazić, A. Violante, K. Cohen, R. Hey, R. Rapaport, and P. V. Santos. Scalable interconnections for remote indirect exciton systems based on acoustic transport. *Phys. Rev. B* **89**, 085313 (2014).

[46] S. de-Leon, Boris Laikhtman. Mott transition, biexciton crossover, and spin ordering in the exciton gas in quantum wells. *Phys. Rev. B* **67**, 235315 (2003).

[47] R. Zimmermann and C. Schindler. Exciton-exciton interaction in coupled quantum wells, *Solid State Commun.* **144**, 395 (2007).

[48] C. Schindler and R. Zimmermann. Analysis of the exciton-exciton interaction in semiconductor quantum wells, *Phys. Rev. B* **78**, 045313 (2008).

[49] Y. E. Lozovik, I. L. Kurbakov, G. E. Astrakharchik, J. Boronat, and M. Willander. Strong correlation effects in 2D Bose-Einstein condensed dipolar excitons, *Solid State Commun.* **144**, 399 (2007).

[50] B. Laikhtman and R. Rapaport. Exciton correlations in coupled quantum wells and their luminescence blue shift, *Phys. Rev. B* **80**, 195313 (2009).

[51] A. L. Ivanov, E. A. Muljarov, L. Mouchliadis, and R. Zimmermann. Comment on Photoluminescence Ring Formation in Coupled Quantum Wells: Excitonic Versus Ambipolar Diffusion. *Phys. Rev. Lett.* **104**, 179701 (2010).

[52] K. Cohen, R. Rapaport, and P. V. Santos. Remote Dipolar Interactions for Objective Density Calibration and Flow Control of Excitonic Fluids, *Phys. Rev. Lett.* **106**, 126402 (2011).

[53] M. Remeika, J. R. Leonard, C. J. Dorow, M. M. Fogler, L. V. Butov, M. Hanson, and A. C. Gossard. Measurement of exciton correlations using electrostatic lattices, *Phys. Rev. B* **92**, 115311 (2015).

[54] Yu. E. Lozovik and O. L. Berman. Phase transitions in a system of two coupled quantum wells, *JETP Lett.* **64**, 573 (1996).

[55] S. De Palo, F. Rapisarda, and G. Senatore. Excitonic Condensation in a Symmetric Electron-Hole Bilayer, *Phys. Rev. Lett.* **88**, 206401 (2002).

[56] G. E. Astrakharchik, J. Boronat, I. L. Kurbakov, and Y. E. Lozovik. Quantum Phase Transition in a Two-Dimensional System of Dipoles, *Phys. Rev. Lett.* **98**, 060405 (2007).

[57] J. Schleede, A. Filinov, M. Bonitz, and H. Fehske. Phase Diagram of Bilayer Electron-Hole Plasmas, *Contrib. Plasma Phys.* **52**, 819 (2012).

[58] R. A. Suris, Gas-Crystal Phase Transition in a 2D Dipolar Exciton System. *J. Exp. Theor. Phys.* **122**, 602 (2016).

[59] M. Y. J. Tan, N. D. Drummond, and R. J. Needs. Exciton and biexciton energies in bilayer systems, *Phys. Rev. B* **71**, 033303 (2005).

[60] A. D. Meyertholen and M. M. Fogler. Biexcitons in two-dimensional systems with spatially separated electrons and holes, *Phys. Rev. B* **78**, 235307 (2008).

[61] R. Maezono, P. López Ríos, T. Ogawa, and R. J. Needs. Excitons and Biexcitons in Symmetric Electron-Hole Bilayers, *Phys. Rev. Lett.* **110**, 216407 (2013).

[62] H. Kadau, M. Schmitt, M. Wenzel, C. Wink, T. Maier, I. Ferrier-Barbut, and T. Pfau. Observing the Rosensweig instability of a quantum ferrofluid, *Nature* (London) **530**, 194 (2016).

[63] I. Ferrier-Barbut, H. Kadau, M. Schmitt, M. Wenzel, and T. Pfau. Observation of Quantum Droplets in a Strongly Dipolar Bose Gas, *Phys. Rev. Lett.* **116**, 215301 (2016).

[64] L. Tanzi, E. Lucioni, F. Famà, J. Catani, A. Fioretti, C. Gabbanini, R. N. Bisset, L. Santos, and G. Modugno. Observation of a Dipolar Quantum Gas with Metastable Supersolid Properties, *Phys. Rev. Lett.* **122**, 130405 (2019).

[65] F. Böttcher, J.-N. Schmidt, M. Wenzel, J. Hertkorn, M. Guo, T. Langen, and T. Pfau. Transient Supersolid Properties in an Array of Dipolar Quantum Droplets, *Phys. Rev. X* **9**, 011051 (2019).

[66] L. Chomaz, D. Petter, P. Ilzhöfer, G. Natale, A. Trautmann, C. Politi, G. Durastante, R. M. W. van Bijnen, A. Patscheider, M. Sohmen, M. J. Mark, and F. Ferlaino. Long-Lived and Transient Supersolid Behaviors in Dipolar Quantum Gases, *Phys. Rev. X* **9**, 021012 (2019).

[67] B. Wunsch, N. T. Zinner, I. B. Mekhov, S.-J. Huang, D.-W. Wang, and E. Demler. Few-Body Bound States in Dipolar Gases and Their Detection, *Phys. Rev. Lett.* **107**, 073201 (2011).

[68] M. Dalmonte, P. Zoller, and G. Pupillo. Trimer Liquids and Crystals of Polar Molecules in Coupled Wires, *Phys. Rev. Lett.* **107**, 163202 (2011).

[69] X. Lu, C.-Q. Wu, A. Micheli, and G. Pupillo. Structure and melting behavior of classical bilayer crystals of dipoles, *Phys. Rev. B* **78**, 024108 (2008).

[70] Safavi-Naini, S. G. Söyler, G. Pupillo, H. R. Sadeghpour, and B. Capogrosso-Sansone. Quantum phases of dipolar bosons in bilayer geometry, *New J. Phys.* **15**, 013036 (2013).

[71] A. Macia, G. E. Astrakharchik, F. Mazzanti, S. Giorgini, and J. Boronat. Single-particle versus pair superfluidity in a bilayer system of dipolar bosons, *Phys. Rev. A* **90**, 043623 (2014).

[72] F. Cinti, D.-W. Wang, and M. Boninsegni. Phases of dipolar bosons in a bilayer geometry, *Phys. Rev. A* **95**, 023622 (2017).

[73] K. Cohen, M. Khodas, B. Laikhtman, P. V. Santos, and R. Rapaport. Vertically coupled dipolar exciton molecules, *Phys. Rev. B* **93**, 235310 (2016).

[74] C. Hubert, Y. Baruchi, Y. Mazuz-Harpaz, K. Cohen, K. Biermann, M. Lemeshko, K.West, L. Pfeiffer, R. Rapaport, and P. Santos. Attractive Dipolar Coupling between Stacked Exciton Fluids, *Phys. Rev. X* **9**, 021026 (2019).

[75] C. Hubert, K. Cohen, A. Ghazaryan, M. Lemeshko, R. Rapaport, and P. V. Santos. Attractive interactions, molecular complexes, and polarons in coupled dipolar exciton fluids, *Phys. Rev. B* **102**, 045307 (2020).

[76] A. T. Hammack, N. A. Gippius, Sen Yang, G. O. Andreev, L. V. Butov, M. Hanson, and A. C. Gossard. Excitons in electrostatic traps, *J. Appl. Phys*. **99**, 066104 (2006).

[77] Y. Y. Kuznetsova, J. R. Leonard, L. V. Butov, J. Wilkes, E. A. Muljarov, K. L. Campman, and A. C. Gossard. Excitation energy dependence of the exciton inner ring, *Phys. Rev. B* **85**, 165452 (2012).

[78] T. Chakraborty. Structure of binary boson mixtures at T = 0 K, *Phys. Rev. B* **26**, 6131 (1982).

[79] S. H. Abedinpour, R. Asgari, and M. Polini. Theory of correlations in strongly interacting fluids of two-dimensional dipolar bosons, *Phys. Rev. A* **86**, 043601 (2012).

[80] L. V. Butov, C. W. Lai, D. S. Chemla, Y. E. Lozovik, K. L. Campman, and A. C. Gossard. Observation of Magnetically Induced Effective-Mass Enhancement of Quasi-2D Excitons, *Phys. Rev. Lett.* **87**, 216804 (2001).

[81] L. V. Butov, V. D. Egorov, V. D. Kulakovskii, and T. G. Anderson. Magnetoluminescence study of many-body effects in a dense electron-hole plasma of strained $In_xGa_{1-x}As$/GaAs quantum wells, *Phys. Rev. B* **46**, 15156 (1992).

[82] M. Sammon and B. I. Shklovskii. Attraction of indirect excitons in van der Waals heterostructures with three semiconducting layers, *Phys. Rev. B* **99**, 165403 (2019).

[83] E. V. Calman, L. H. Fowler-Gerace, D. J. Choksy, L. V. Butov, D. E. Nikonov, I. A. Young, S. Hu, A. Mishchenko, and A. K. Geim. Indirect Excitons and Trions in MoSe$_2$/WSe$_2$ van der Waals Heterostructures, *Nano Lett.* **20**, 1869 (2020).

[84] L.V. Butov, V.D. Kulakovskii, E. Lach, A. Forchel, D. Grutzmacher. Magnetoluminescence study of many-body effects in homogeneous quasi-two-dimensional electron-hole plasma in undoped InGaAs/InP single quantum wells, *Phys. Rev. B* **44**, 10680 (1991).

[85] G. D. Mahan. Excitons in Degenerate Semiconductors. *Phys. Rev.* **153**, 882 (1967).

[86] M.S. Skolnick, J.M. Rorison, K.J. Nash, D.J. Mowbray, P.R. Tapster, S.J. Bass, A.D. Pitt. Observation of a Many-Body Edge Singularity in Quantum-Well Luminescence Spectra, *Phys. Rev. Lett.* **58**, 2130 (1987).

[87] L. Kappei, J. Szczytko, F. Morier-Genoud, B. Deveaud. Direct Observation of the Mott Transition in an Optically Excited Semiconductor Quantum Well, *Phys. Rev. Lett.* **94**, 147403 (2005).

[88] L.V. Butov, A.L. Ivanov, A. Imamoglu, P.B. Littlewood, A.A. Shashkin, V.T. Dolgopolov, K.L. Campman, A.C. Gossard. Stimulated scattering of indirect excitons in coupled quantum wells: Signature of a degenerate Bose-gas of excitons, *Phys. Rev. Lett.* **86**, 5608 (2001).

[89] S. Ben-Tabou de-Leon, B. Laikhtman. Exciton-exciton interactions in quantum wells: Optical properties and energy and spin relaxation, *Phys. Rev. B* **63**, 125306 (2001).

[90] L.V. Keldysh. The electron-hole liquid in semiconductors, Contemp. Phys. **27**, 395 (1986).

[91] K. Sivalertporn, L. Mouchliadis, A.L. Ivanov, R. Philp, E.A. Muljarov. Direct and indirect excitons in semiconductor coupled quantum wells in an applied electric field, *Phys. Rev. B* **85**, 045207 (2012).

[92] C. Comte, P. Noziéres. Exciton Bose condensation: the ground state of an electron-hole gas -I. Mean field description of a simplified model, *J. de Physique* **43**, 1069 (1982).

[93] M.M. Fogler, Sen Yang, A.T. Hammack, L.V. Butov, A.C. Gossard. Effect of spatial resolution on the estimates of the coherence length of excitons in quantum wells, *Phys. Rev. B* **78**, 035411 (2008).

[94] M.M. Fogler, L.V. Butov, K.S. Novoselov. High-temperature superfluidity with indirect excitons in van der Waals heterostructures, *Nat. Commun.* **5**, 4555 (2014).

[95] M.M. Dignam, J.E. Sipe. Exciton states in coupled double quantum wells in a static electric field, *Phys. Rev. B* **43**, 4084 (1991).

[96] Jacques Des Cloizeaux. Exciton instability and crystallographic anomalies in semiconductors, *J. Phys. Chem. Solids* **26**, 259 (1965).

[97] A.N. Kozlov, L.A. Maksimov. The metal-dielectric divalent crystal phase transition, Sov. Phys. JETP 21, 790 (1965).

[98] D. Jerome, T.M. Rice, W. Kohn, Excitonic Insulator, Phys. Rev. 158, 462 (1967).

[99] J.P. Eisenstein, A.H. MacDonald, Bose-Einstein condensation of excitons in bilayer electron Systems, Nature 432, 691 (2004).

[100] M. Rontani, L.J. Sham, Coherent Transport in a Homojunction between an Excitonic Insulator and Semimetal, Phys. Rev. Lett. 94, 186404 (2005).

[101] L. Du, X. Li, W. Lou, G. Sullivan, K. Chang, J. Kono, R.-R. Du, Evidence for a topological excitonic insulator in InAs/GaSb bilayers, Nat. Commun. 8, 1971 (2017).

[102] A. Kogar, Melinda S. Rak, Sean Vig, Ali A. Husain, Felix Flicker, Young Il Joe, Luc Venema, Greg J. MacDougall, Tai C. Chiang, Eduardo Fradkin, Jasper van Wezel, Peter Abbamonte, Signatures of exciton condensation in a transition metal dichalcogenide, Science 358, 1314 (2017).

[103] X. Liu, K. Watanabe, T. Taniguchi, B. I. Halperin, P. Kim, Quantum Hall drag of exciton condensate in graphene, Nat. Phys. 13, 746 (2017).

[104] J.I.A. Li, T. Taniguchi, K.Watanabe, J. Hone, C.R. Dean, Excitonic superfluid phase in double bilayer graphene, Nat. Phys. 13, 751 (2017).

[105] G. W. Burg, N. Prasad, K. Kim, T. Taniguchi, K. Watanabe, A. H. MacDonald, L. F. Register, E. Tutuc, Strongly Enhanced Tunneling at Total Charge Neutrality in Double-Bilayer Graphene-WSe$_2$ Heterostructures, *Phys. Rev. Lett.* **120**, 177702 (2018).

[106] Z. Sun, T. Kaneko, D. Golez, A. J. Millis, Second-Order Josephson Effect in Excitonic Insulators, *Phys. Rev. Lett.* **127**, 127702 (2021).

[107] S. Samaneh Ataei, D. Varsano, E. Molinari, M. Rontani, Evidence of ideal excitonic insulator in bulk MoS2 under pressure, *PNAS* **118**, e2010110118 (2021).

[108] K. Kim, H. Kim, J. Kim, C. Kwon, J. S. Kim, B. J. Kim, Direct observation of excitonic instability in Ta$_2$NiSe$_5$, *Nat. Commun*. **12**, 1969 (2021).
[109] X. Liu, J.I.A. Li, K. Watanabe, T. Taniguchi, J. Hone, B. I. Halperin, P. Kim, C. R. Dean, Crossover between strongly coupled and weakly coupled exciton superfluids, *Science* **375**, 205 (2022).

[110] Y. Jia, P. Wang, C.-L. Chiu, Z. Song, G. Yu, B. Jack, S. Lei, S. Klemenz, F. A. Cevallos, M. Onyszczak, N. Fishchenko, X. Liu, G. Farahi, F. Xie, Y. Xu, K. Watanabe, T. Taniguchi, B. A. Bernevig, R. J. Cava, L. M. Schoop, A. Yazdani, S. Wu, Evidence for a monolayer excitonic insulator, *Nat. Phys.* **18** 87 (2022).

[111] B. Sun, W. Zhao, T. Palomaki, Z. Fei, E. Runburg, P. Malinowski, X. Huang, J. Cenker, Y.-T. Cui, J.-H. Chu, X. Xu, S. S. Ataei, D. Varsano, M. Palummo, E. Molinari, M. Rontani, D. H. Cobden, Evidence for equilibrium exciton condensation in monolayer WTe2, *Nat. Phys.* **18**, 94 (2022).

[112] J. Gu, L. Ma, S. Liu, K. Watanabe, T. Taniguchi, J. C. Hone, J. Shan, K. F. Mak, Dipolar excitonic insulator in a moiré lattice, *Nat. Phys.* **18**, 395 (2022).

[113] Z. Zhang, E. C. Regan, D. Wang, W. Zhao, S. Wang, M. Sayyad, K. Yumigeta, K. Watanabe, T. Taniguchi, S. Tongay, M. Crommie, A. Zettl, M. P. Zaletel, F. Wang, Correlated interlayer exciton insulator in heterostructures of monolayer WSe2 and moiré WS_2/WSe_2, *Nat. Phys.* **18**, 1214 (2022).

[114] D. Chen, Z. Lian, X. Huang, Y. Su, M. Rashetnia, L. Ma, L. Yan, M. Blei, L. Xiang, T. Taniguchi, K. Watanabe, S. Tongay, D. Smirnov, Z. Wang, C. Zhang, Y.-T. Cui, S.-F. Shi, Excitonic insulator in a heterojunction moiré superlattice. *Nat. Phys.* **18**, 1171 (2022).

[115] M. W. Zwierlein, J.R. Abo-Shaeer, A. Schirotzek, C.H. Schunck, W. Ketterle, Vortices and superfluidity in a strongly interacting Fermi gas, *Nature* **435**, 1047 (2005).

[116] P.T. Landsberg, Electron Interaction Effects on Recombination Spectra, *Phys. Stat. Sol.* **15**, 623 (1966).

[117] S. Das Sarma, Y. Liao, Know the enemy: 2D Fermi liquids, *Annals of Physics* **435**, 168495 (2021).

[118] M. Combescot, P. Nozi´eres, Infrared catastrophy and excitons in the X-ray spectra of metals, *J. de Physique* **32**, 913 (1971).

[119] J.S. Lee, Y. Iwasa, N. Miura, Observation of the Fermi edge anomaly in the absorption and luminescence spectra of n-type modulation-doped GaAs-AlGaAs quantum wells, *Semicond. Sci. Technol.* **2**, 675 (1987).

[120] Abriela Livescu, David A.B. Miller, D.S. Chemla, M. Ramaswamy, T.Y. Chang, Nicholas Sauer, A.C. Gossard, J.H. English, Free Carrier and Many-Body Effects in Absorption Spectra of Modulation-Doped Quantum Wells, *IEEE J. Quantum Electronics* **24**, 1677 (1988).

[121] K. Ohtaka, Y. Tanabe, Golden-rule approach to the soft-x-ray-absorption problem. V. Thermal broadening and comparison with experiments in quantum wells, *Phys. Rev. B* **39**, 3054 (1989).

[122] T. Uenoyama, L. J. Sham, Effect of Finite Hole Mass on Edge Singularities in Optical Spectra, *Phys. Rev. Lett.* **65**, 1048 (1990).

[123] P. Hawrylak, Optical properties of a two-dimensional electron gas: Evolution of spectra

from excitons to Fermi-edge singularities, *Phys. Rev. B* **44**, 3821 (1991).

[124] A. Zrenner, P. Leeb, J. Schafler, G. Bohm, G. Weimann, J. M. Worlock, L.T. Florez, J.P. Harbison, Indirect excitons in coupled quantum well structures, *Surf. Sci.* **263**, 496 (1992).

[125] M. Alloing, M. Beian, M. Lewenstein, D. Fuster, Y. Gonzalez, L. Gonzalez, R. Combescot, M. Combescot, F. Dubin, Evidence for a Bose-Einstein condensate of excitons, *Europhys. Lett.* **107**, 10012 (2014).

[126] M. Stern, V. Umansky, I. Bar-Joseph, Exciton Liquid in Coupled Quantum Wells, *Science* **343**, 55 (2014).

[127] F. Fedichkin, P. Andreakou, B. Jouault, M. Vladimirova, T. Guillet, C. Brimont, P. Valvin, T. Bretagnon, A. Dussaigne, N. Grandjean, P. Lefebvre, Transport of dipolar excitons in (AlGa)N/GaN quantum wells, *Phys. Rev. B* **91**, 205424 (2015).

[128] Kobi Cohen, Yehiel Shilo, Ken West, Loren Pfeiffer, Ronen Rapaport, Dark High Density Dipolar Liquid of Excitons, *Nano Lett.* **16**, 3726 (2016).

[129] A.V. Gorbunov, V.B. Timofeev, Coherence of Bose-Einstein condensates of dipolar excitons in GaAs/AlGaAs heterostructures, *Low Temp. Phys.* **42**, 340 (2016).

[130] W.J. Skocpol, M. Tinkham, "Fluctuations near superconducting phase transitions," *Rep. Prog. Phys.* **38**, 1049 (1975).

[131] L.G. Aslamazov, A.I. Larkin, Effect of fluctuations on properties of a superconductor above critical temperature, *Sov. Phys. Solid State* **10**, 875 (1968).

[132] S. Schmitt-Rink, C. Ell, H. Haug, Many-body effects in the absorption, gain, and luminescence spectra of semiconductor quantum-well structures, *Phys. Rev. B* **33**, 1183 (1986).

[133] B.I. Halperin, T.M. Rice, The Excitonic State at the Semiconductor-Semimetal Transition, *Solid State Physics* **21**, 115 (1968).